

# Martian water ice clouds during the 2018 global dust storm as observed by the ACS-MIR channel onboard the Trace Gas Orbiter

A. Stcherbinine<sup>1,2</sup>, M. Vincendon<sup>1</sup>, F. Montmessin<sup>2</sup>, M. J. Wolff<sup>3</sup>, O. Korablev<sup>4</sup>, A. Fedorova<sup>4</sup>, A. Trokhimovskiy<sup>4</sup>, A. Patrakeev<sup>4</sup>, G. Lacombe<sup>2</sup>, L. Baggio<sup>2</sup>, A. Shakun<sup>4</sup>

<sup>1</sup>Institut d'Astrophysique Spatiale, Université Paris-Saclay, CNRS, 91405 Orsay, France

<sup>2</sup>LATMOS/IPSL, UVSQ Université Paris-Saclay, Sorbonne Université, CNRS, 78280 Guyancourt, France

<sup>3</sup>Space Science Institute, 4750 Walnut Street, Suite 205, Boulder, Colorado, 80301, USA

<sup>4</sup>Space Research Institute (IKI), 84/32 Profsoyuznaya, 117997 Moscow, Russia

## Key Points:

- Monitoring of Martian water ice clouds and derivation of vertical profiles of particle size using the 3  $\mu\text{m}$  spectral band.
- Observation of mesospheric water ice clouds at altitudes  $\geq 90$  km during the MY 34 GDS.
- Evidence of water ice particles  $\geq 1.5$   $\mu\text{m}$  between 50 km and 70 km during the GDS.

arXiv:1912.08018v2 [astro-ph.EP] 18 Feb 2020

**Abstract**

The Atmospheric Chemistry Suite (ACS) instrument onboard the ExoMars Trace Gas Orbiter (TGO) ESA-Roscosmos mission began science operations in March 2018. ACS Mid InfraRed (MIR) channel notably provides solar occultation observations of the martian atmosphere in the 2.3 – 4.2  $\mu\text{m}$  spectral range. Here we use these observations to characterize water ice clouds before and during the MY 34 Global Dust Storm (GDS). We developed a method to detect water ice clouds with mean particle size  $\leq 2 \mu\text{m}$ , and applied it to observations gathered between  $L_s = 165^\circ$  and  $L_s = 243^\circ$ . We observe a shift in water ice clouds maximum altitudes from about 60 km before the GDS to above 90 km during the storm. These very high altitude, small-sized ( $r_{\text{eff}} \leq 0.3 \mu\text{m}$ ) water ice clouds are more frequent during MY34 compared to non-GDS years at the same season. Particle size frequently decreases with altitude, both locally within a given profile and globally in the whole dataset. We observe that the maximum altitude at which a given size is observed can increase during the GDS by several tens of km for certain sizes. We notably notice some large water ice particles ( $r_{\text{eff}} \geq 1.5 \mu\text{m}$ ) at surprisingly high altitudes during the GDS (50 – 70 km). These results suggest that GDS can significantly impact the formation and properties of high altitude water ice clouds as compared to the usual perihelion dust activity.

**Plain Language Summary**

In this article, we use data from the Atmospheric Chemistry Suite (ACS) infrared spectrometer onboard the European Space Agency (ESA)-Roscosmos Exomars Trace Gas Orbiter (TGO) mission to study water ice clouds in the Martian atmosphere. More specifically, we aim to characterize the evolution of their altitude, geographic distribution and microphysical properties before and during the planet-wide dust storm that occurred during the summer of 2018. In particular, we developed a method to simultaneously detect the water ice clouds and constrain their particle size using simulated spectra of water ice. We observe that the maximal altitude of the clouds increased from 60 km to above 90 km during the storm. Most high altitude clouds have small particle sizes (lower than 0.3 microns) as expected from the low pressure at such altitude. However, we also observe for the first time large (larger than 1.5 microns) water ice particles at unusually high altitude (higher than 60 km), uniquely during the storm. This suggests that the increased atmospheric activity associated with global dust storm significantly impacts water ice clouds formation.

**1 Introduction**

Since the first spectroscopic detection by Mariner 9 (Hanel et al., 1972), water ice clouds have been extensively studied because of their connection to the Martian water cycle (Clancy et al., 1996; Madeleine et al., 2012; Smith et al., 2013; Clancy et al., 2017; Guzewich & Smith, 2019). Clouds scatter and absorb incoming solar radiation, thus impacting atmospheric structure and temperature. As a result, water ice cloud particles can modify the global circulation of the Martian atmosphere (Wilson et al., 2008). Clouds are also a major actor in the inter-hemispheric water exchange (Clancy et al., 1996). As the evolution of our understanding of the martian climate shows an increasing role of water ice clouds, there is a growing need to better characterize the properties of water ice aerosols in order to better understand and model Mars climate and weather (Richardson, 2002; Montmessin et al., 2004; Navarro et al., 2014). Recent studies have notably reveal how more precise vertical representation of water-related atmospheric phenomena may impact water cycle modeling (Vals et al., 2018). Precise observational constraints about the actual microphysical properties of clouds as a function of altitude, notably particle size, are thus of interest to better characterize the whole water cycle.

Planetary-scale storms, characterized by widespread lifting and transport of dust particles, modify the thermodynamics and circulation of the Martian atmosphere on a global scale, and subsequently affect the water cycle. While regional dust storms are recurrent phenomena on Mars, few of them evolve into events that encircle the whole planet to become global dust storms (hereafter "GDS"). Such events are erratic, with an average of one occurrence every three to four Martian years (Zurek & Martin, 1993; Clancy et al., 2000; D. M. Kass et al., 2016). The first two GDSs of the 21<sup>st</sup> century occurred 6 Earth years apart, in 2001 and 2007, corresponding to Martian Years (hereafter "MY") 25 and 28 (e.g. Wang & Richardson, 2015). Two large (regional) dust storms developed in 2018 (MY 34): one in the Northern hemisphere starting at  $L_s = 181^\circ$ , and the other in the Southern hemisphere at  $L_s = 188^\circ$ . They subsequently merged to become a GDS at  $L_s = 193^\circ$ , lasting until  $L_s = 250^\circ$  (Guzewich et al., 2019; Sánchez-Lavega et al., 2019; Smith, 2019). This GDS occurred near the Northern fall equinox, however, it should be noted that there is no unique timing for the onset and development of GDSs on Mars. For instance, the MY 28 GDS, occurred significantly later, at the end of the so-called storm season (from  $L_s = 260^\circ$  to  $L_s = 310^\circ$ ) (Wang & Richardson, 2015). This variability implies that a variety of scenarios dictate the formation of GDSs, requiring individual assessments of GDS's.

The MY 28 dust storm has been shown to have profoundly influenced the water vapor atmospheric distribution, elevating water well above the troposphere ( $>60$  km) (Fedorova et al., 2018) while pushing up the hygropause altitude (Heavens et al., 2018). A rapid increase of the H<sub>2</sub>O and HDO abundances at altitudes between 40 and 80 km (Vandaele et al., 2019) was observed during MY 34 storm, and recently reproduced in a GCM simulation (Neary et al., 2019). This large augmentation of the high altitude water content is believed to boost hydrogen, or nearly equivalently, water escape from Mars (Chaffin et al., 2017; Heavens et al., 2018; Fedorova et al., 2020). However, the formation of clouds impacts the ability of water (or hydrogen) to escape as it confines (in theory) a significant fraction of water below the cloud level. Thus, understanding the extent to which high altitude water vapor condenses to form clouds during GDSs is important in assessing the possible propagation pathways of water vapor up to the exobase (Neary et al., 2019). Because water vapor can exist in a supersaturated state in the Martian atmosphere (Maltagliati et al., 2011) and has been observed in a large amount during the MY 34 GDS (Fedorova et al., 2020), simply supposing that the freezing point can be used to set the limits where water is free to be mobilized is likely to be problematic. The availability of condensation nuclei, supplied by the ubiquitous atmospheric dust particles, and possibly by interplanetary dust particles and micrometeoritic smoke that aggregates as entering the Martian atmosphere (Crismani et al., 2017; Plane et al., 2018; Hartwick et al., 2019), is another key factor controlling the potential for water ice clouds. It has for example been shown by a number of studies (Michelangeli et al., 1993) that the occurrence of supersaturation is anti-correlated to the availability of condensation nuclei. The condensation nuclei themselves are expected to be much more abundant during GDS, including with larger sizes (e.g. Wolff & Clancy, 2003; Clancy et al., 2010; Lemmon et al., 2019), which may impact how and when water ice clouds form. It is however difficult to predict the distribution and properties of condensation nuclei at high altitude during GDS, which additionally modify the thermal structure of the atmosphere. In this complex situation, accumulating observational constraints about the actual behavior of water ice at high altitude during GDS is required to provide further constraints on the fate of high altitude water vapor during these events.

The ExoMars Trace Gas Orbiter (TGO), ESA-Roscosmos Atmospheric Chemistry Suite (ACS) and Nadir and Occultation for Mars Discovery (NOMAD) instruments started their science operation phase in March 2018 (Korablev et al., 2018; Vandaele et al., 2018; Korablev et al., 2019; Vandaele et al., 2019), before the MY 34 GDS. The ACS middle-infrared (MIR) channel is a crossed-dispersion echelle spec-

trometer dedicated to solar occultation (hereafter, "SO"): each observation covers a  $\sim 300$  nm wide spectral interval selected between 2.3 and 4.2  $\mu\text{m}$ . This interval is set by rotating the spectrometer secondary grating (i.e., the diffraction order separation) to align the interval of interest with the detector. The cross-dispersion aspect provides from 10 to 21 diffraction orders (spectral segments) stacked on top of each other. The separation between consecutive orders is only dependent on the number of orders displayed at once and thus on the secondary grating position. Thirteen different positions can be employed to completely sample the full accessible spectral range of the instrument. With the two hours orbital period of TGO and the performing of SO in the mid-infrared, ACS and NOMAD provides a totally new and huge dataset of vertical profiles of the atmospheric extinction (Korablev et al., 2018; Vandaele et al., 2018). We are using the ACS-MIR channel to study the extinction properties of the Martian airborne particles in the 3  $\mu\text{m}$  spectral region, which possesses a distinct diagnostic capability to identify the O-H stretching signature; whether it is due to water ice absorption or bound water in dust. In the case of water ice, the depth and shape of the feature depend on both the abundance and the particle size of water ice (Vincendon et al., 2011; Guzewich et al., 2014; Clancy et al., 2019). The ACS-MIR occultation data in this spectral range gives us complementary information to those derived from previous limb and nadir scattered light observations by OMEGA (Bibring et al., 2004; Vincendon et al., 2011) and CRISM (Murchie et al., 2007; Clancy et al., 2019; Guzewich et al., 2014). We focus here on the use of the water ice absorption feature during the MY 34 GDS that offer a relevant framework for a further characterization of the interactions between water and dust during extreme dust events.

## 2 Data analysis

In order to study the 3  $\mu\text{m}$  water ice absorption band, we use the instrument configuration centered on the 3.1 – 3.4  $\mu\text{m}$  spectral range corresponding to the 12th secondary grating position. Figure 1 presents the spatial and temporal distribution of the position 12 MIR observations used in this study, covering a temporal range from  $L_s = 165^\circ$  to  $L_s = 243^\circ$ . However, due to the SO geometry, observations only occur in the periods near local times of 06:00AM and 06:00PM.

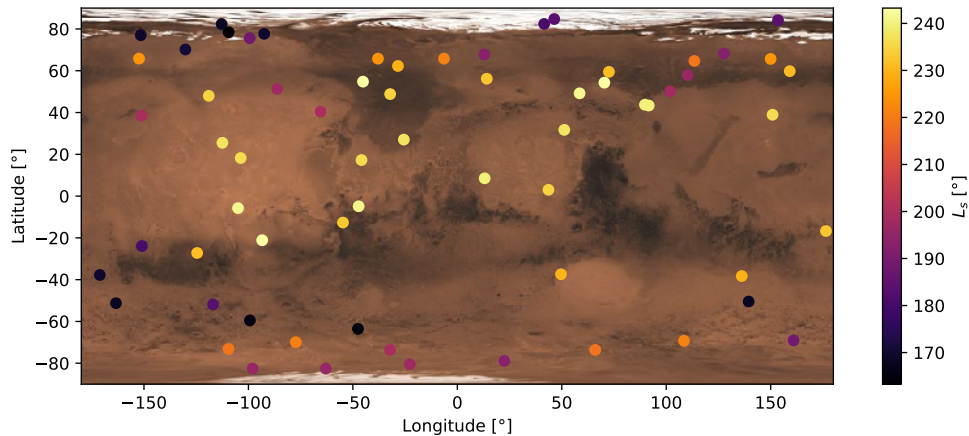


**Figure 1.** Spatial and time distribution of the 65 ACS-MIR observations used in this study.

## 2.1 Continuum extraction

Every ACS-MIR observation is composed of  $\sim 20$  spectral segments individually exhibiting broad instrumental shapes that generally prevents contiguous segments from matching precisely in their overlapping wavelength intervals (cf. figure 2) due to instrumental effects (Korablev et al., 2018; Trokhimovskiy et al., 2015). As the aerosol property derivation is intrinsically dependent of the continuum behavior, we have adopted a method to extract the continuum across all displayed fraction orders, taking into account this spectral shape of each order. This allows us to derive the continuum shape across the 3 to 3.4  $\mu\text{m}$  range.

In order to do this, we have chosen to fit the 200 centered spectral points of each diffraction order with a 2<sup>nd</sup> degree polynomial, and use an iterative method to remove the gas absorption bands that tend to bias the continuum values represented by the fitted polynomial. After the first iteration, for each diffraction order we determine the standard deviation of the transmission values of the considered spectral points  $\sigma$ , and we consider that all the points with transmission lower than the polynomial fit by at least  $\sigma$  (i.e.  $\text{Tr}(\lambda) < (\text{fit}(\lambda) - \sigma)$ ) are affected by some gas absorption. So we remove these points as they tend to underestimate the actual continuum. In a second step, we perform the same filtering method from a polynomial fit on each diffraction order for the remaining wavelengths (i.e. the 200 centered points without the ones with transmission values lower than  $(\text{fit} - \sigma)$ ). Finally, we perform a third fit to the continuum and then only retain the fitted transmission value at the center point of each fitted order (cf. figure 2.b). As a result, the complete spectrum has an effective spectral resolution of one point per diffraction order, which corresponds to a spectral resolution of  $\sim 1 - 2$  nm. This is a much smaller number of points than the ACS-MIR native sampling, but is sufficient to capture the general shape of the continuum used in the next sections for solid particles characterisation. Next, we estimate the uncertainties of the data as the sum of the standard deviation of the difference between the data and the polynomial fit for each order (*random uncertainties*), and the maximal gap between the polynomial fit of the order and the extracted continuum (1 point per order), linearly interpolated between each diffraction order (*systematic uncertainties* due to the curvature of the diffraction orders, see figure 2.c). Additionally, in the following we do not consider the outer regions of the spectra in order to avoid detector edge effects, i.e. the spectels corresponding to 3.10, 3.12 and 3.44  $\mu\text{m}$ .

## 2.2 Haze top determination

Using this extracted continuum at each observed tangent point, we can determine the haze top altitude for each observation. We define haze top as the highest altitude at which aerosols can be sensed along the line of sight. We calculate haze top by finding the first altitude for which the transmission is greater than a defined threshold  $(1 - \varepsilon)$ .  $\varepsilon$  introduces the consideration of the artificial non-steady nature of the measured transmission as it approaches unity at high altitude. We observe empirically that this transition occurs above transmissions around 0.99. We have thus selected a conservative value of  $\varepsilon = 0.02$  for this threshold. An example is provided in the figure 3.

## 2.3 3 $\mu\text{m}$ band monitoring

The 3  $\mu\text{m}$  absorption feature corresponds to the OH/H<sub>2</sub>O absorption. We quantify the depth of this feature as a function of altitude using an Integrated Band Depth (IBD) method (Jouglet et al., 2007; Calvin, 1997). This approach computes the mean depth of transmission between two selected wavelengths (see eq. 1 and figure 4).

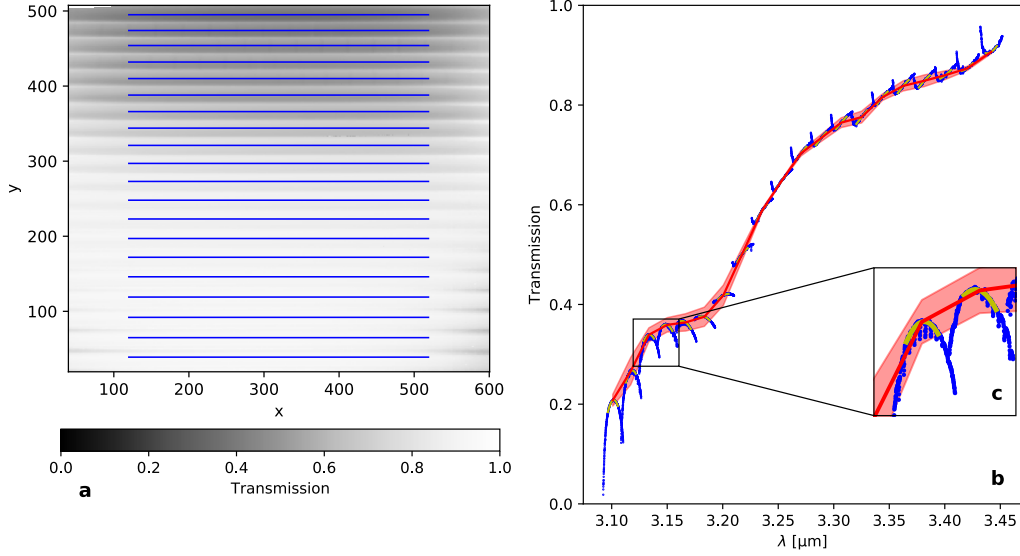


**Figure 2.** Extraction of the spectral continuum. **a.** Reduced calibrated image of the ACS-MIR detector containing 20 diffraction orders along the y-axis. For each order, the wavelength varies along the x-axis. Each blue line corresponds to the detector pixels used to obtain the spectrum of one diffraction order. **b.** Corrections steps for the extraction of the spectral continuum. In blue the initial data, in yellow the polynomial fit of the 200 points from the center of each order (after the third iteration), and in red the extracted continuum (with the associated uncertainties in the red shadowed region). **c.** Zoom on two diffraction orders.

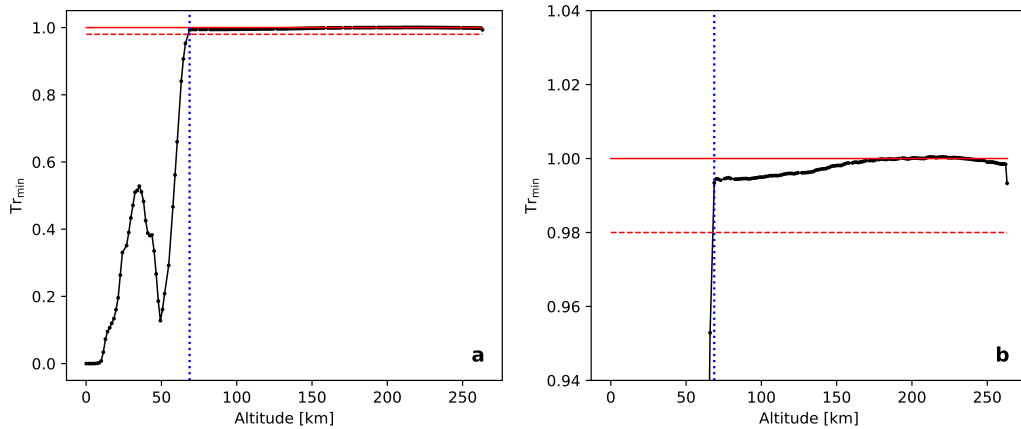


**Figure 3.** Haze top determination. **a.** Example of transmission spectra as a function of altitude. The red lines correspond respectively to transmission levels of 1 (solid line) and 0.98 (dashed line). **b.** Zoom on the plateau reached for transmissions greater than about 0.99. A conservative threshold of 0.98 corresponding to  $\varepsilon = 0.02$  has been selected to calculate the haze top altitude shown by the blue dotted line (69 km in this example).

$$\text{IBD}(\text{Tr}, \lambda_1, \lambda_2) = \frac{1}{\lambda_2 - \lambda_1} \int_{\lambda_1}^{\lambda_2} [\text{Tr}(\lambda_2) - \text{Tr}(\lambda)] d\lambda \quad (1)$$

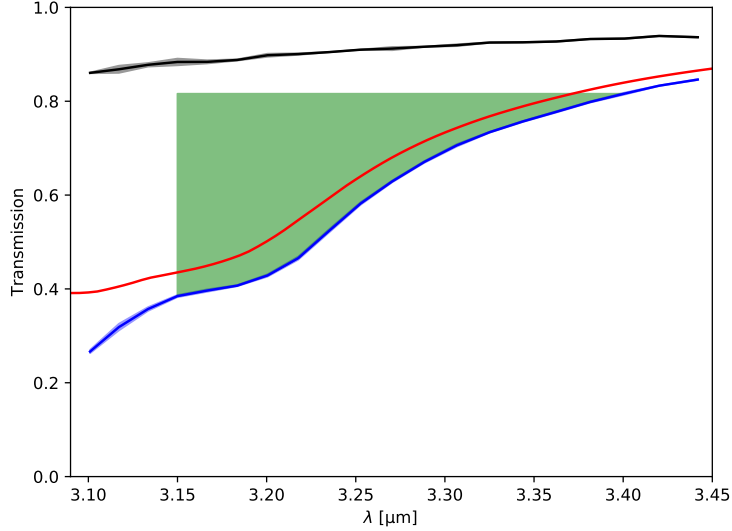


**Figure 4.** Calculation of the 3  $\mu\text{m}$  Integrated Band Depth (IBD) which can be used as a first order proxy for the presence of some water ice clouds. In blue, we show an example of ACS-MIR position 12 spectra, showing a strong 3  $\mu\text{m}$  absorption band. In green is shown the measurement of the 3  $\mu\text{m}$  absorption using the IBD method (cf. equation (1)) with  $\lambda_1 = 3.15 \mu\text{m}$  and  $\lambda_2 = 3.4 \mu\text{m}$ ). This spectrum is compared to the theoretical transmission of 0.5  $\mu\text{m}$  spherical water ice particles in red (see section 3.1) and in black, another example of ACS-MIR spectra with a low 3  $\mu\text{m}$  band, and presumably no water ice.

## 2.4 Extinction coefficient determination

In order to retrieve the extinction profile and properties of the aerosols, we employ a vertical inversion algorithm based on the onion-peeling method (Goldman & Saunders, 1979), from the total optical depth  $\tau$  (i.e., as integrated along the line of sight). The result is the the extinction coefficient  $k_{\text{ext}}$  as a function of altitude. Then, we can compute the opacity of a cloud by integrating the extinction coefficient along a vertical line between the boundary altitudes detected for the cloud (see the following sections for a description of the water ice clouds identification).

For each altitude level  $i$ , the optical depth is given by:

$$\tau_i(\lambda) = \sum_{j=i}^N 2 \times \underbrace{\left( \sqrt{R_{j+1}^2 - R_i^2} - \sqrt{R_j^2 - R_i^2} \right)}_{A_{i,j}} k_{\text{ext},j}(\lambda) \quad (2)$$

That we can rewrite in a matrix manner:

$$\tau = A k_{\text{ext}} \quad (3)$$

The transfer matrix  $A$  is upper triangular so it is invertable and we can write :

$$k_{\text{ext}} = A^{-1} \tau \quad (4)$$

I.e.

$$k_{\text{ext},i} = \sum_{j=i}^N (A^{-1})_{i,j} \tau_j \quad (5)$$

Then, according to BIMP et al. (2008), as  $\tau = -\log(\text{Tr})$  and  $k_{\text{ext}}$  given as a function of  $\tau$  in (5), we have the uncertainties on the optical depth values (6) and their propagation to the extinction coefficient  $k_{\text{ext}}$  throughout the vertical inversion given by (7).

$$\Delta\tau(\lambda) = \frac{\Delta\text{Tr}(\lambda)}{\text{Tr}(\lambda)} \quad (6)$$

$$\Delta(k_{\text{ext},i}) = \sqrt{\sum_{j=i}^N (A^{-1})_{i,j}^2 (\Delta\tau_j)^2} \quad (7)$$

## Notation

$N$  The number of atmospheric layers.

$\text{Tr}_i$  The measured transmission value at the  $i^{\text{th}}$  altitude.

$\tau_i$  The optical depth observed at the  $i^{\text{th}}$  altitude (integrated along the line of sight).

$k_{\text{ext},i}$  The extinction coefficient of the  $i^{\text{th}}$  atmospheric layer.

$R_i$  The radius of the sphere corresponding to the bottom altitude of the  $i^{\text{th}}$  atmospheric layer, i.e. the altitude of the bottom of the layer added to the Martian radius.

Figure 5 presents several examples of retrieved vertical profiles of the extinction coefficient  $k_{\text{ext}}$  from ACS-MIR observations before and during the MY 34 GDS. We can already notice the presence of one or several detached layers in some profiles, which are located at various altitudes. We also observe strong spectral variability between observations, with some layers having a distinctive signature when comparing the transmissions at 3.2 and 3.4  $\mu\text{m}$  (compare e.g. blue and red profiles in panels a and d of figure 5). We will discuss in the next section how this spectral behavior can be modeled to derive information about the presence and properties of water ice clouds.

## 3 Water ice cloud modeling

### 3.1 Model and hypothesis

In order to identify water ice clouds, and constrain their particle sizes, we have computed the wavelength dependence of the extinction coefficient of pure water ice and dust layers of various particle sizes (figure 6). These extinction coefficients are calculated using a public domain Mie code (Toon & Ackerman, 1981) and assuming a gamma size distribution (Hansen & Travis, 1974) with an effective variance of 0.1 (e.g. Wolff et al., 2017, and references contained within).

We can see in the figure 6 that the spectral properties of water ice and dust differ significantly in most cases, and that there is a strong dependence of the spectral shape on particle size for water ice. This is not true when water ice particles sizes become greater than about 3  $\mu\text{m}$ : for such sizes the absorption become quite flat in the 3.1 – 3.5  $\mu\text{m}$  range whatever the particle size and it is even not possible to differentiate water ice from dust. Particles size lower than 0.1  $\mu\text{m}$  have similar  $k_{\text{ext}}$  spectra corresponding to the Rayleigh diffusion regime. As a consequence, we do not make any distinction between water ice particles with radii of 0.1  $\mu\text{m}$  and lower.

In the following, we fit our retrieved extinction coefficient from ACS data to these models for pure water ice or dust layers in order to identify and characterize water ice rich layers composed of particles lower than  $\sim 2 \mu\text{m}$ , as results suggesting larger water



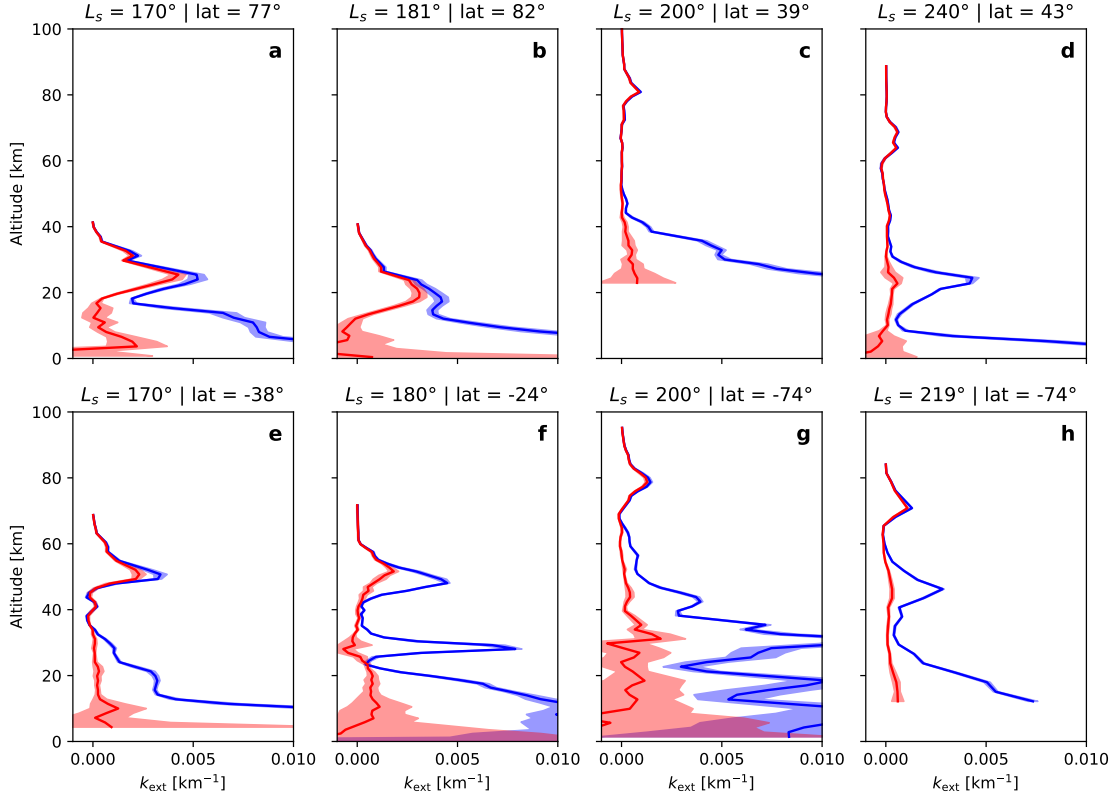


**Figure 5.** Typical extinction coefficient vertical profiles retrieved from different ACS-MIR observations. In **blue** the extinction coefficient at  $3.2 \mu\text{m}$ , which provides a proxy for the overall particle (dust and ice) profile. In **red** the difference between the extinction coefficient at  $3.2 \mu\text{m}$  and  $3.4 \mu\text{m}$ , which provides a proxy for the presence of band depth associated with small-grained water ice. We can see layers with various behavior, some typical of the presence of small-grained water ice (e.g., e at about 50 km) and some interpreted as resulting from either large-grained water ice, or dust (e.g., d at 20 km). See section 4 for discussion. The shadows regions show the uncertainties on the  $k_{\text{ext}}$  values.

ice particles are eliminated in the filtering process due to possible confusion with dust (see section 3.3). Layers not identified as such can correspond to either dust-dominated or large-grained water ice layers.

### 3.2 Water ice particle size retrieving method

As the extinction opacity  $C_{\text{ext}}$  is proportional to  $k_{\text{ext}}$ , we try to fit our ACS-MIR  $k_{\text{ext}}$  data with the modeled  $C_{\text{ext}}$  spectra. To do this, we consider the extinction coefficient as a function of the wavelength  $\lambda$ , the effective radius  $r_{\text{eff}}$  and a scalar factor  $\alpha > 0$  (cf. equation (8)), where  $\alpha$  is related to the number of particles that have scattered the light and  $C_{\text{ext}}^{\text{interp}}$  is interpolated from the input models, using a bivariate spline approximation. The distinction between  $k_{\text{ext}}$  and  $C_{\text{ext}}$  is just a matter of normalization ( $\frac{C_{\text{ext}}(\lambda, r_{\text{eff}})}{C_{\text{ext}}(\lambda_0, r_{\text{eff}})} = \frac{k_{\text{ext}}(\lambda, r_{\text{eff}})}{k_{\text{ext}}(\lambda_0, r_{\text{eff}})}$ ). However, we decide to leave  $\alpha$  as a free parameter to get rid of the choice of normalization wavelength  $\lambda_0$ .

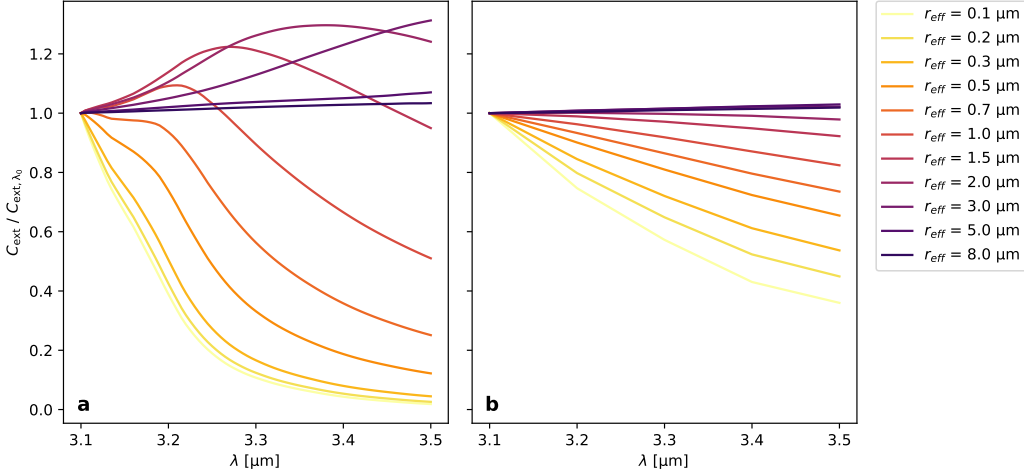


**Figure 6.** Water ice and dust models. **a.** Simulated extinction opacity spectra  $C_{\text{ext}}(\lambda)$  for water ice spherical particles of different sizes, normalized at  $\lambda_0 = 3.1 \mu\text{m}$ . **b.** Same plot for dust spherical particles. For particles with  $r_{\text{eff}} > 3 \mu\text{m}$ , we cannot distinguish between water ice and dust signature in this spectral window.

$$k_{\text{ext}}(\lambda, r_{\text{eff}}, \alpha) = \alpha C_{\text{ext}}^{\text{interp}}(\lambda, r_{\text{eff}}) \quad (8)$$

Then, in order to avoid the problem of the presence of local minima for  $r_{\text{eff}}$  in the *least-square* fitting algorithm, we generate models on a grid of radii of  $0.01 \mu\text{m}$  between  $0.1 \mu\text{m}$  and  $8 \mu\text{m}$ , and for each one we retrieve the optimal value of  $\alpha$  using the *Trust Region Reflective algorithm* implemented in the `scipy.optimize.curve_fit()` Python function (Virtanen et al., 2019). Thus, we obtain the best fit for each particle size, that we compare in a second time, by computing a  $\chi^2$  from the data and the model, as defined in the equation (9) (Bevington & Robinson, 1992). This allows us to find the global minimum of  $\chi^2$  as a function of the particle size, and derive the associated  $r_{\text{eff}}$  with this "best fit".

$$\chi^2(r_{\text{eff}}) = \sum_{i=1}^N \frac{(\text{data}_i - \text{model}_{r_{\text{eff}}, i})^2}{\sigma_i^2} \quad (9)$$

Finally, we use the reduced chi-square  $\chi_\nu^2$  defined in the equation (10), as a measure of the goodness of the fit (Bevington & Robinson, 1992). In theory, a model is considered to be a good approximation of the data when  $\chi_\nu^2 \leq 1$ .

$$\chi_\nu^2(r_{\text{eff}}) = \frac{1}{N-2} \sum_{i=1}^N \frac{(\text{data}_i - \text{model}_{r_{\text{eff}}, i})^2}{\sigma_i^2} = \frac{\chi^2}{\nu} \quad (10)$$

## Notation

**data<sub>i</sub>** The  $i^{\text{th}}$  spectral of the  $k_{\text{ext}}$  spectra from the ACS-MIR observation.

**model<sub>r<sub>eff</sub>, i</sub>** The  $i^{\text{th}}$  spectral of the model extinction spectra for a particle size of  $r_{\text{eff}}$ .

**$\sigma_i$**  The uncertainty on the value of  $\text{data}_i$ .

- $N$  The number of spectral points in the considered spectrum.
- $\nu$  The number of degrees of freedom ( $\nu = N - p$ ).
- $p$  The number of fitting parameters (here  $p = 2$ ).

Then, in order to quantify the uncertainties for the retrieved particles size, we search for the  $r_{\text{eff}}$  of all the models that will pass our filtering criteria (cf section 3.3) during the fitting process of an ACS-MIR spectrum and verify  $\chi_{\nu, \text{ice}}^2 \leq (2\chi_{\nu, \text{ice}, \text{min}}^2 + 1)$ , where  $\chi_{\nu, \text{ice}, \text{min}}^2$  is the minimal value of  $\chi_{\nu, \text{ice}}^2$  (i.e. associated with the optimal  $r_{\text{eff}}$  value). This last criteria that essentially affects low  $\chi_{\nu, \text{ice}}^2$  values was added to take into account the goodness of the optimal fit in the uncertainties estimation. As all these models can be considered as acceptable, they will define the uncertainties range of the fit. In other words, the optimal  $r_{\text{eff}}$  corresponds to the model with the lower  $\chi_{\nu, \text{ice}}^2$  value, and the lower (respectively upper) bounds for the particle size uncertainties corresponds to the minimal (respectively maximal) value of  $r_{\text{eff}}$  in the set of models that prove equation (11) along with  $\chi_{\nu, \text{ice}}^2 \leq (2\chi_{\nu, \text{ice}, \text{min}}^2 + 1)$ .

### 3.3 Filtering of dust/ice ambiguous cases

We identify water ice clouds by correlating extinction coefficient spectral behavior compatible with water ice, and incompatible with dust. To do that, we experimentally determined  $\chi^2$  thresholds that we present in the following. Thus, to be classified unambiguously as a water ice cloud detection, a layer needs to have a  $\chi_{\nu}^2 \leq 9$  for water ice, but also a lower quality fit to dust. We then apply the previously described fitting algorithm also for dust and not only for water ice. We eliminate all those observations that the water ice models don't improve the  $\chi_{\nu}^2$  by at least a factor 4, as well as the ones that it is possible to fit a dust spectra with a  $\chi_{\nu}^2 \leq 1$ . That is to say, we only consider the fits which verify the condition (11). This last criteria was added as a safeguard and is relevant in the case of a fit associated to a low  $\chi_{\nu}^2$  value, where even if  $\chi_{\nu, \text{dust}}^2 \geq 4\chi_{\nu, \text{ice}}^2$ , the dust model still provide a good fit of the data that we cannot ignore.

$$(\chi_{\nu, \text{ice}}^2 \leq 9) \ \& \ \left( \chi_{\nu, \text{ice}}^2 \leq \frac{\chi_{\nu, \text{dust}}^2}{4} \right) \ \& \ (\chi_{\nu, \text{dust}}^2 > 1) \quad (11)$$

In addition, we also remove the fits whose error bars exceed a pre-defined threshold of 0.35  $\mu\text{m}$ . An example of such a fit is found in figure 7.j. However, in most cases, such poorly constrained fits were already eliminated through the dust-fitting test (figure 7.k).

After this multi-step filtering process, we note that retrieved particle sizes never exceed 2  $\mu\text{m}$ ; in essence the fits indicating sizes between 2  $\mu\text{m}$  and 8  $\mu\text{m}$  have been removed, which was expected as the extinction coefficient is not diagnostic of water ice in that size range, as discussed previously. As a consequence, it is appropriate to consider that our method makes it possible to identify and characterize water ice rich layers with mean particle size of  $\sim 2$   $\mu\text{m}$  maximum. Other layers can correspond to either dust-dominated or large-grained water ice layers.

## 4 Results and discussion

### 4.1 The 3 $\mu\text{m}$ atmospheric absorption

The atmospheric 3  $\mu\text{m}$  integrated band depth can be used to obtain a quick look at water ice clouds in our dataset. It is also of interest in itself as orbital observations of Mars surface have to account for atmospheric 3  $\mu\text{m}$  contribution to deliver information

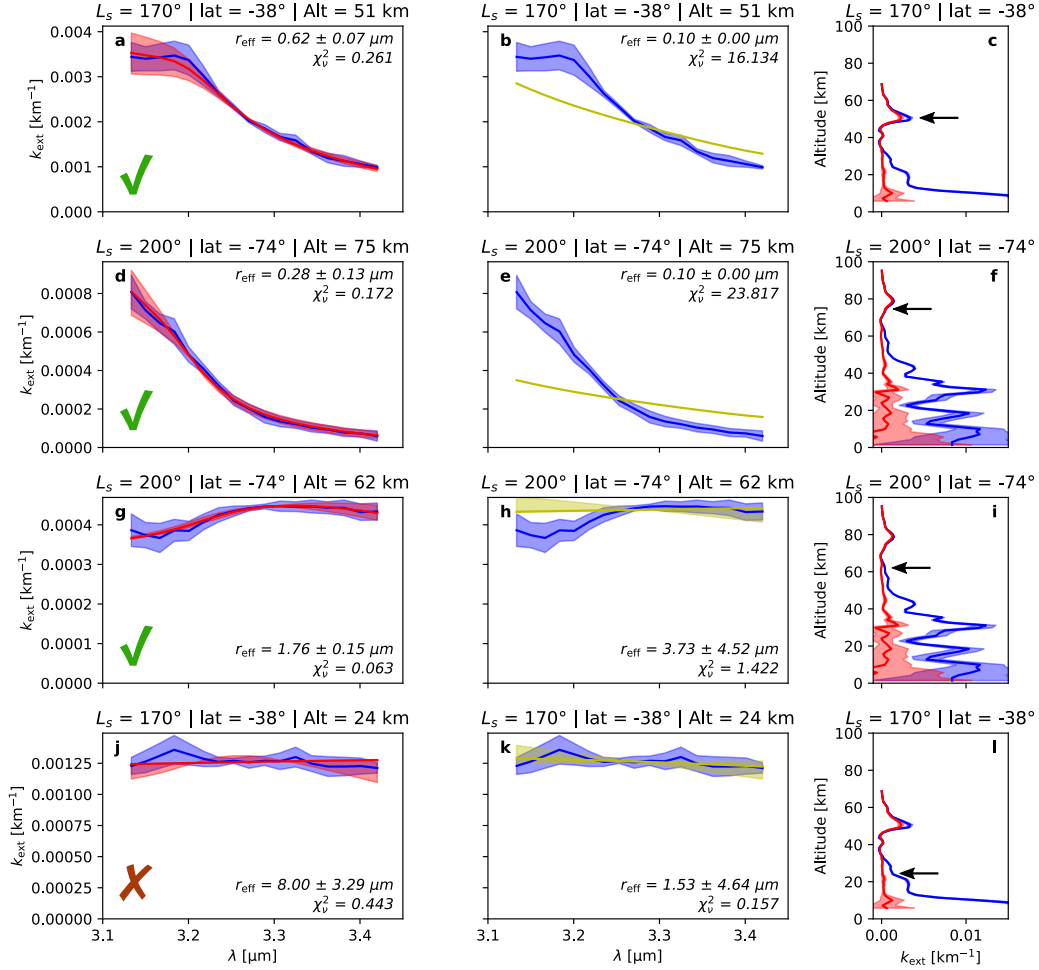


**Figure 7.** Water ice cloud identification and particle size retrievals from ACS-MIR  $k_{\text{ext}}$  spectra. The two first columns shows the results of the fitting algorithm using the water ice model (left column) or the dust model (center column). The blue area represents the ACS-MIR spectra, while the red and yellow lines represent respectively the best fit using the water ice and dust models. The right column shows for each observation (line) the associated  $k_{\text{ext}}$  vertical profile (in blue the extinction coefficient at  $3.2 \mu\text{m}$ , and in red the difference between the extinction coefficient at  $3.2 \mu\text{m}$  and  $3.4 \mu\text{m}$ ). The black arrows indicate the altitude of the extracted spectrum. We observe that even if all the presented spectra can be reproduced by our water ice model, the fourth case (j) remains ambiguous as the dust model is also able to provide a acceptable fit (k). Thus, we will accept the three first fits a, d & g while the fit j will be rejected by the filtering process.

about surface hydration (Jouglet et al., 2007; Audouard et al., 2014). As illustrated in figure 8, the  $3 \mu\text{m}$  IBD matches at first order the more elaborated water ice detection scheme presented in section 3. Actually, the  $3 \mu\text{m}$  IBD captures only small-grained ( $r_{\text{eff}} \leq 1 \mu\text{m}$ ) water ice clouds according to modeling results presented in figure 6, but this corresponds to typically 90% of detected clouds here (see figures 13 & 15). In addition, the IBD does not capture thin clouds that produce a tenuous absorption, whatever their grain size. Thus, thin layers (normal integrated layer optical depth

lower than 0.01) that can be observed at very high altitudes ( $\geq 90$  km) are not always discernible with IBD figures. Beside these slight differences, the IBD criteria thus illustrates the overall water ice pattern and provide a proxy for the optical thickness of clouds. We have illustrated the overall behavior of water ice clouds using figure 9 where the  $3 \mu\text{m}$  IBD variations are represented from  $L_s = 165^\circ$  to  $L_s = 243^\circ$  in the Northern (a) and Southern (c) hemispheres.

We observe in figure 9 that some vertical profiles corresponding to observations acquired at close  $L_s$  and are so overlapping in the figure can manifest notable differences in the  $3 \mu\text{m}$  IBD criterion. This probably reflects actual variations between profiles, associated with longitudinal variations of the water ice clouds (Smith, 2004; Wolff et al., 2019), as illustrated in table 1. Local time differences (Szantai et al., 2019) may also contribute to the variability (Table 1), although the dataset is not yet extensive enough to properly delineate local time effects.

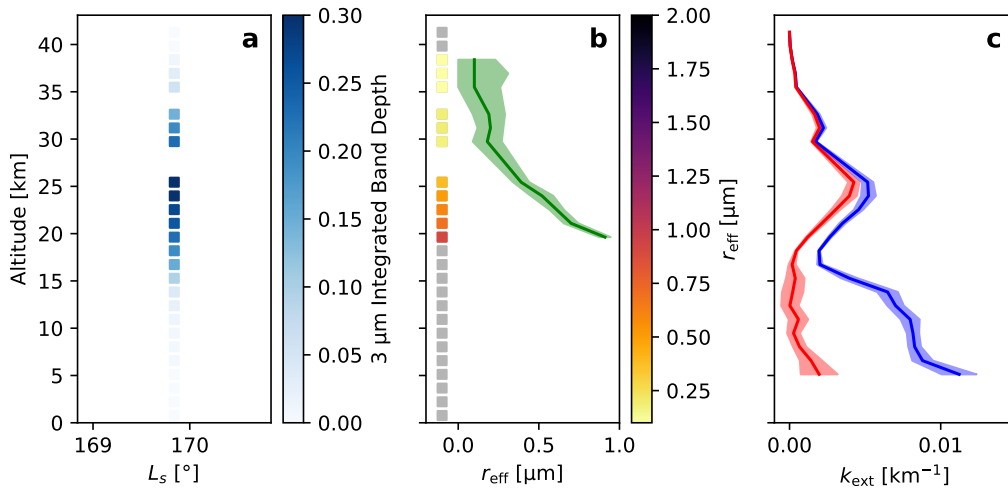


**Figure 8.** Vertical profile of a water ice cloud ( $L_s = 169.8^\circ$ ,  $\text{lat} = 77^\circ\text{N}$ ,  $\text{lon} = 152^\circ\text{W}$ ), showing the vertical variations of the IBD (a), particle size (b) and the extinction coefficient (c), with in blue the extinction coefficient at  $3.2 \mu\text{m}$ , and in red the difference between the extinction coefficient at  $3.2 \mu\text{m}$  and  $3.4 \mu\text{m}$ . We observe that the IBD criterion detects the same water ice cloud as the fitting methodology, and that the size of the water ice particles of the cloud decrease as the altitude increases (b): from  $1.2 \mu\text{m}$  at  $18$  km to  $0.2 \mu\text{m}$  at  $31$  km.

## 4.2 Clouds monitoring

Using the method presented in section 3, we can both detect the presence of water ice clouds layers in the Martian atmosphere and retrieve their particle size (see discussion in section 4.5). Figure 10 presents the resulting vertical profiles of water ice particles from  $L_s = 165^\circ$  to  $L_s = 243^\circ$  in the Northern and Southern hemispheres. This overview reveals two main trends in our dataset. First, we detect water ice clouds in most observations. In more detail, in our dataset of 65 ACS-MIR grating position-12 observations, 11 of them have no water ice cloud detection, i.e., 83% of our profiles show at least one detection of water ice. Non-detections are localized in time and places: 45% of our non-detections are located at the onset of the GDS ( $193^\circ \leq L_s \leq 198^\circ$ , 5 observations), and the other 55% are located during the GDS ( $219^\circ \leq L_s \leq 231^\circ$ , 6 observations) but corresponds to low haze top altitude beyond the northern limit

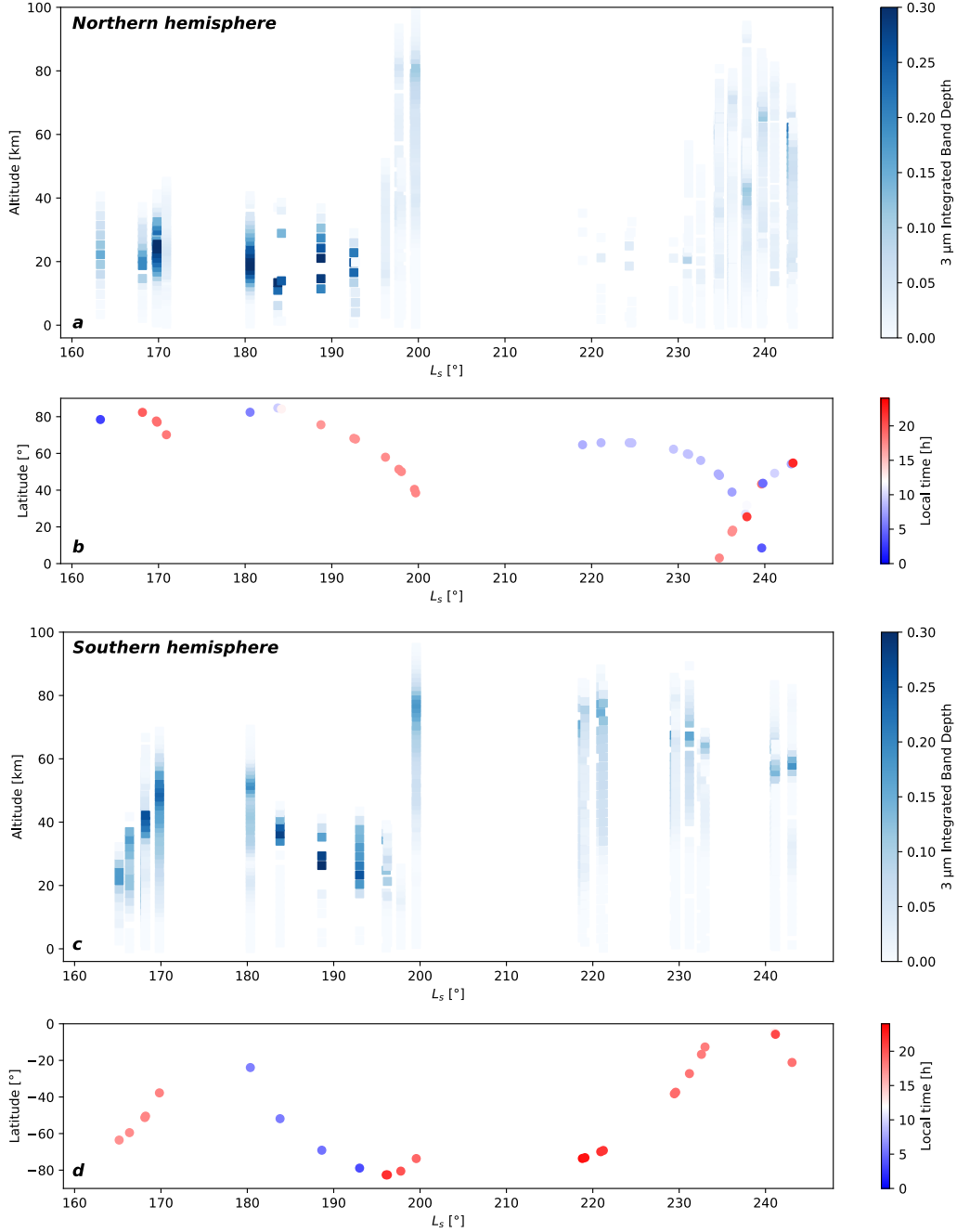


**Figure 9.** 3 μm water ice absorption band (IBD) monitoring from the ACS MIR channel in the Martian Northern (a) and Southern (c) hemisphere, before and during the 2018 GDS (MY 34). Latitude and local time of observations are indicated in panels b & d

of the GDS (see detailed discussion in section 4.4). Second, we observe the presence of two distinct types of vertical profiles that correspond to the two periods separated by the sudden onset of the GDS at  $L_s \sim 195^\circ - 200^\circ$  (Guzewich et al., 2019). Two main cloud characteristics differ between these two periods: the vertical extent, and the water ice cloud opacity. Most of the detected clouds are between 10 km and 70 km

$L_s$	Latitude	Longitude	Local time	Observation
168.1°	51°S	<b>163°W</b>	17h39	<i>No IBD</i>
168.2°	50°S	<b>139°E</b>	17h40	<i>IBD ~ 0.25 at 40 km</i>
192.6°	68°N	<b>28°E</b>	17h09	<i>IBD ~ 0.26 at 20 km</i>
192.7°	68°N	<b>3°E</b>	17h09	<i>No IBD</i>
229.4°	38°S	<b>136°E</b>	18h53	<i>IBD ~ 0.18 at 65 km</i>
229.6°	37°S	<b>50°E</b>	18h52	<i>No IBD</i>
243.1°	54°N	<b>70°E</b>	<b>07h50</b>	<i>IBD ~ 0.22 at 60 km</i>
243.3°	55°N	<b>45°W</b>	<b>22h10</b>	<i>No IBD</i>

**Table 1.** Identification of consecutive observations with and without 3  $\mu\text{m}$  atmospheric absorption using the IBD, showing the local aspect of our observed clouds (see the vertical IBD profiles in figure 9). The first three examples are associated with significant variations in longitude, while the last example also show strong local time variations.

before the onset of the GDS, while clouds altitudes typically extend higher between 60 km and about 90 km afterward. Figure 12 shows the vertical profiles of  $k_{\text{ext}}$  at 3.4  $\mu\text{m}$  (i.e. the opacity per km). As 3.4  $\mu\text{m}$  is on the edge of the 3  $\mu\text{m}$  water ice band (Vincendon et al., 2011) it provides an estimator of the global atmospheric opacity, whereas the opacity at 3.2  $\mu\text{m}$  is strongly increased by the presence of water ice clouds. We observe that the water ice clouds opacity at 3.2  $\mu\text{m}$  (vertically integrated along the cloud) typically goes from 0.01 to 0.05 before the GDS, but falls to a few  $10^{-3}$  for the mesospheric clouds during the GDS, with  $k_{\text{ext}}(\lambda = 3.2 \mu\text{m}) \sim 10^{-4} \text{ km}^{-1}$  around 90 km (and  $k_{\text{ext}}(\lambda = 3.4 \mu\text{m}) \sim 10^{-5} \text{ km}^{-1}$ ). We discuss in more details the distribution and properties of clouds during these two periods in the next two sections.

### 4.3 Before the GDS ( $L_s < 195^\circ$ )

Before the dust storm, we observe the presence of water ice clouds in most profiles, with altitudes ranging from 11 to 44 km in the Northern hemisphere, and between 17 and 69 km in the Southern hemisphere, which is consistent with previous observations (Smith et al., 2013). Thus, clouds are found below the mesosphere for most of the cases. However, the latitude coverage of available observations in the North and in the South are not equivalent (cf. figure 10): Northern observations prior to the GDS are restricted to polar latitudes  $\geq 68^\circ$ .

During this period, we indeed observe a latitude-dependence of the haze top altitude that increases closer to the equator (up to  $\sim 70$  km at  $24^\circ\text{S}$ ) and decreases when moving towards polar latitudes (down to  $\sim 40$  km at  $80^\circ\text{N}$ , or  $60^\circ\text{S}$ ), see also figure 11.a. This trend is consistent with the expected haze top behavior (Jaquin et al., 1986; Forget et al., 1999; Montmessin et al., 2006; Heavens et al., 2011; Smith et al., 2013). However, the lack of data around the equatorial latitudes before the GDS (no observations between  $20^\circ\text{S}$  and  $60^\circ\text{N}$ , see figure 11.a) prevents us to get access to the latitude of the maximum haze top altitude.

Water ice clouds are detected in the upper parts of most profiles, but some profiles also include lower detached layers (e.g. figure 5.f at 30 km) that are not detected either by the fitting process or the IBD (as the  $k_{\text{ext}}$  at 3.2  $\mu\text{m}$  and 3.4  $\mu\text{m}$  are similar). Thus, these layers are likely be either composed primarily of dust or by  $> 2 \mu\text{m}$  water ice particles (cf. section 3.3). This suggests that water ice appears to frequently cap the dust layer in our solar longitude range (Smith et al., 2013). Note however that larger-

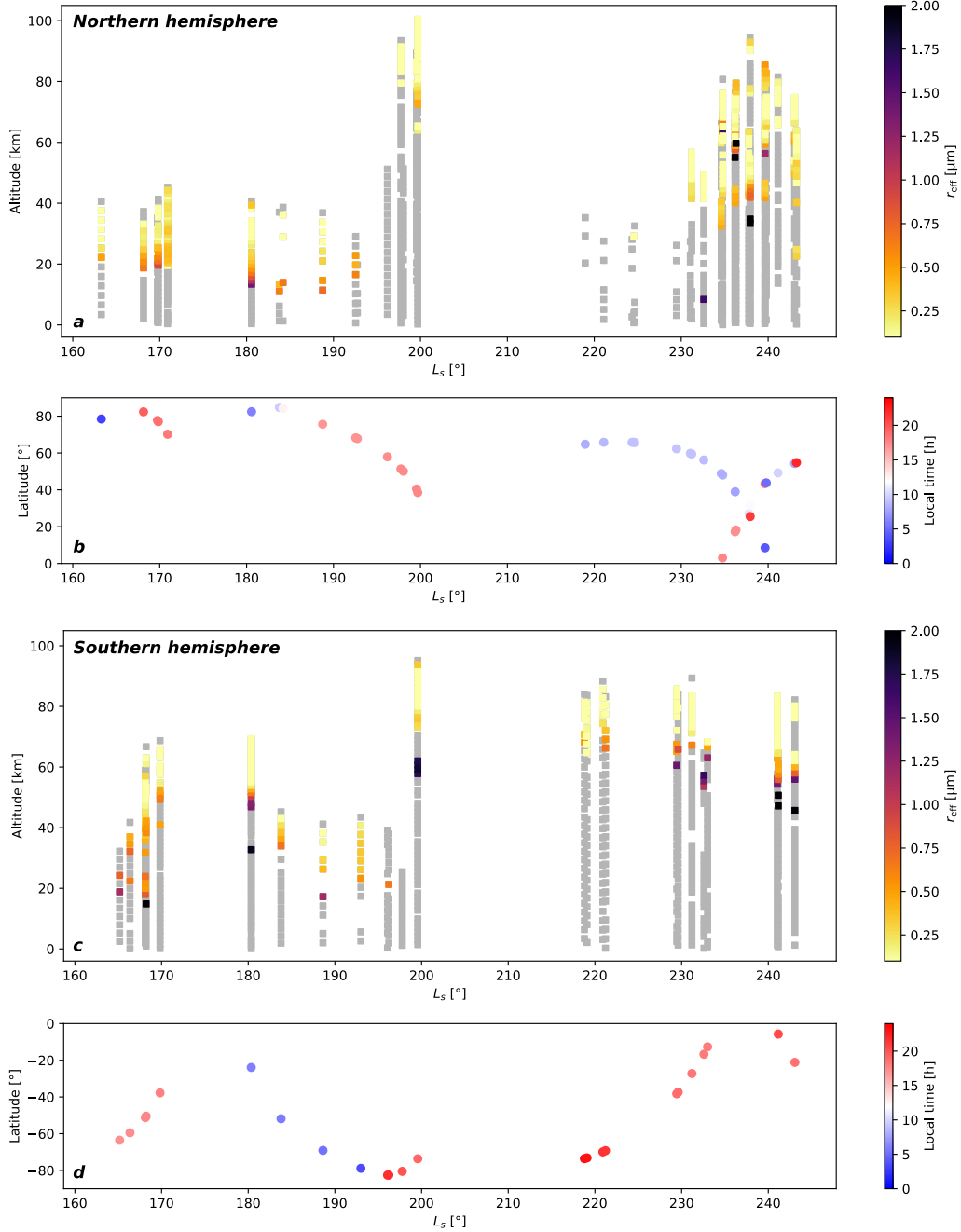


**Figure 10.** Vertical profiles of the retrieved size of the water ice particles in the Martian Northern (a) and Southern (c) hemispheres, before and during the MY 34 GDS. In grey the observations without water ice detection. Latitude and local time of the observations are indicated in panels b & d.

grained water ice clouds can also be present at lower altitude (Wolff & Clancy, 2003), but remain undetected here due to a lack of a clear signature in our spectral range (as discussed previously). Nevertheless, the altitude distribution of the detected water ice clouds follows a similar latitudinal trend as the haze top itself: the average altitude



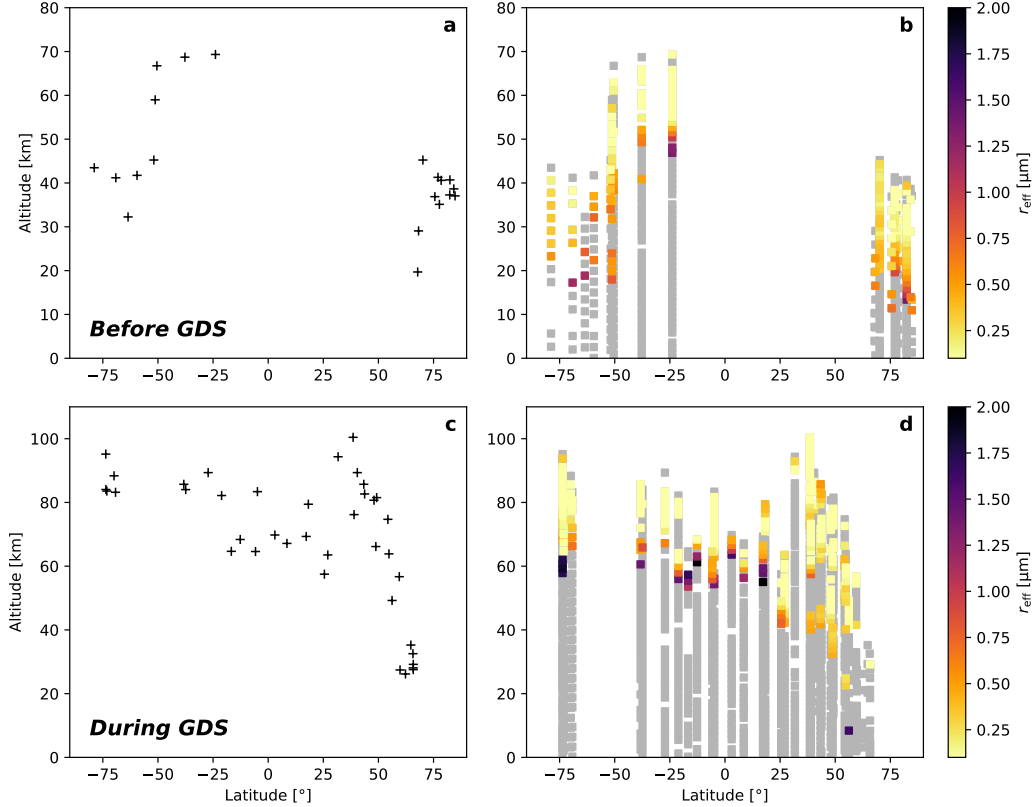


**Figure 11.** **a.** The altitude of the haze top as a function of latitude for the observations before the MY 34 GDS ( $163^\circ \leq L_s \leq 195^\circ$ ). We observe a latitude dependence of the haze top which increases equatorwards in the Southern hemisphere. Unfortunately, all the observations of the Northern hemisphere during these period are concentrated at high latitudes. **b.** The vertical profiles of  $r_{\text{eff}}$  as a function of latitude for the same observations. In the Southern hemisphere, we observe that the water ice clouds altitude seems to follow the same latitudinal trend of the haze top in the equatorial region. **c. & d.** Same as a. & b. but during the MY 34 GDS ( $199^\circ \leq L_s \leq 244^\circ$ ).

of cloud detection prior the dust storm increases equatorward (cf. figure 11.b), as previously noticed by Kleinböhl et al. (2009) and Smith et al. (2013).

#### 4.4 During the GDS ( $L_s > 200^\circ$ )

Around  $L_s = 200^\circ$ , there is a sudden increase in the altitudes of both the haze top (up to 100 km) and the water ice clouds ( $\geq 90$  km), while geographical coordinates remain essentially the same ( $83^\circ\text{S}$  and  $58^\circ\text{N}$  at  $L_s = 196^\circ$ , and  $74^\circ\text{S}$  and  $39^\circ\text{N}$  at  $L_s = 200^\circ$ ). These behaviors are combined with a decrease of the measured IBD values (cf. figure 9). We note that the above behavior appears to be relatively uniform around the planet (i.e., both zonally and meridionally). Specifically, in the Southern hemisphere, even though the observed latitude varies from  $74^\circ\text{S}$  to  $5^\circ\text{S}$  between  $L_s = 219^\circ$  and  $L_s = 241^\circ$ , one does not see a change in both the haze top altitude and the maximal altitude of the water ice clouds; in agreement with the simulations presented in Neary et al. (2019, Figure 3). We nonetheless identify a temporal trend likely related to the progressive decay of the dust storm (Guzewich

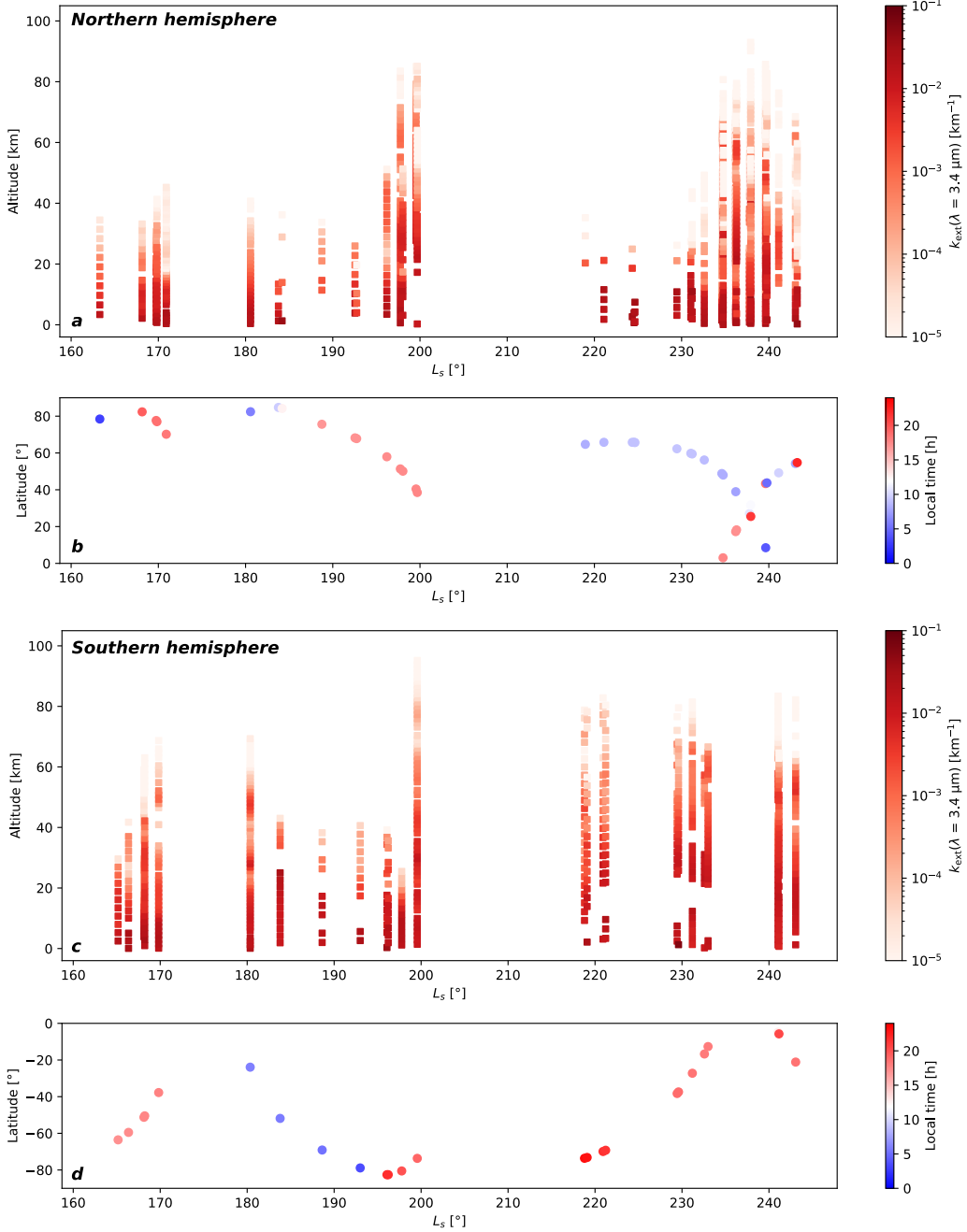


**Figure 12.** Vertical profiles of the measured opacity ( $k_{\text{ext}} = d\tau/dz$ ) at  $3.4 \mu\text{m}$  in the Martian Northern (a) and Southern (c) hemispheres, before and during the MY 34 GDS. Latitude and local time of the observations are indicated in panels b & d.

et al., 2019): from  $L_s = 220^\circ$  to  $L_s = 243^\circ$  the lower altitude of the detected water ice clouds in the Southern hemisphere decrease from 68 km to 54 km (cf. figure 10) and the main  $3 \mu\text{m}$  atmospheric absorption (i.e. the maximum of IBD for a given profile) decrease from 75 km to 58 km (cf. figure 9). Regardless that the haze top altitude remains at  $\sim 85 - 90$  km, and the latitude goes successively towards and from the equator. Nevertheless, we note a slight North/South asymmetry during the dust

storm that is represented by the smaller number of high-altitude water ice clouds in the Northern hemisphere (see figure 11.c&d).

Ice clouds are detected at very high altitudes in the mesosphere during this period, up to  $\geq 80$  km at the beginning of the GDS. A few profiles show robust water detections at altitudes above 90 km, up to 100 km maximum at  $L_s \sim 200^\circ$  (cf. figure 14.c). These high altitude water ice clouds are observed only at the beginning of the GDS. High altitude water ice clouds can also be seen during non-dust GDS years, when they occur during the storm season (Vincendon et al., 2011; Clancy et al., 2019). However, high cloud altitudes are nearly systematic in our observations during the peak phase of the GDS (cf. figure 10), while such altitudes are less typical during non-GDS years (Clancy et al., 2019). Moreover, peak cloud altitudes are slightly higher during the onset of the GDS than reported in non-GDS years. Indeed, models (Neary et al., 2019) showed that GDS are expected to slightly increase the average and maximum altitude of water ice clouds, which is consistent with our observations. The sharp increase in water ice cloud altitude observed during the GDS indeed confirms that this water ice cloud increase is directly connected to dust storm activity. The large-scale dust storm probably facilitates the formation of high altitude water ice clouds through increase in the altitude of both water vapor and condensation nuclei. This increase of water ice altitude during the GDS is indeed consistent with the recently reported increase of water vapor at higher altitudes (Fedorova et al., 2018; Neary et al., 2019).

We still observe a North/South latitudinal asymmetry during the GDS. In the Northern hemisphere, seven observations in the figure 11.c exhibit low haze top altitudes during the GDS. The haze top is between 26 km and 36 km, i.e.  $\sim 50$  km below the altitudes measured during the dust storm for most of the other profiles. Actually, these profiles were taken at high Northern latitude ( $60^\circ\text{N} - 66^\circ\text{N}$ ) during the decay of the dust storm ( $L_s = 221^\circ - 231^\circ$ ) at longitudes of  $\sim 25^\circ\text{W}$  (Acidalia Planitia) and  $\sim 155^\circ\text{E}$  (Utopia Planitia), see table 2: this suggests that  $60^\circ\text{N}$  represents the Northern extent of the dust storm activity in these regions from  $L_s \sim 220^\circ$ , which is in agreement with MCS measurements (D. Kass et al., 2019). The scheme is different for the Southern hemisphere, with high haze top altitudes ( $> 80$  km) observed during the GDS up to the polar regions ( $73^\circ\text{S}$ ).

$L_s$	Latitude	Longitude	Local time	Haze top altitude
219.0°	65°N	113°E	08h14	35.3 km
221.1°	66°N	6°W	08h38	27.5 km
224.3°	66°N	38°W	09h07	28.1 km
224.6°	66°N	152°W	09h09	29.2 km
224.7°	66°N	150°E	09h09	32.5 km
229.5°	62°N	28°W	09h16	26.2 km
231.1°	60°N	159°E	09h06	27.4 km

**Table 2.** Properties of profiles located outside the GDS beyond its Northern limit at  $L_s \sim 225^\circ$ . With a mean haze top altitude of 30 km, i.e. 50 km lower other measurements during the same period, these observations can no longer be considered as part of the GDS. These low haze top observations are located at latitudes greater than  $60^\circ$  with some longitudinal variability. This latitude thus correspond to the Northern maximum extent of the GDS at that time, in agreement with MCS measurements (D. Kass et al., 2019).

#### 4.5 Particle size

We observe that the particle size decreases on average with increasing altitude (cf. figure 13), as previously reported by Clancy et al. (2019). This global trend is also apparent in the majority of individual profiles: particle size is observed to decrease with altitude within a given cloud as we can see in figure 14. This is true regardless of the average altitude of the considered cloud (cf. figure 14). The distribution of particle size as a function of altitude is globally shifted to higher altitudes during the GDS (cf. figure 13), i.e., a given size of particles can go higher in the atmosphere during the GDS. Clancy et al. (2019) also observe a similar trend during non-GDS years, with a given class of particle size that increases in altitude during the perihelion season ( $L_s = 180 - 340^\circ$ ).

While trends can be identified on a global scale, some variability is also evident, as seen in figure 15. As the main clouds altitude increases, water ice particles become distinctly smaller in the storm, with a median effective radius of  $0.28 \mu\text{m}$  before the dust storm and  $\leq 0.1 \mu\text{m}$  during it. This narrower range of smaller particles, with a strong peak for  $r_{\text{eff}} \leq 0.2 \mu\text{m}$ , is typical of the mesospheric clouds (Clancy et al., 2019, figure 12).

Additionally, we also observe the appearance of a small population of larger water ice particles, with  $r_{\text{eff}} \geq 1.5 \mu\text{m}$ , at surprisingly high altitude (between 55 km and 64 km) in view of previous observations and studies (e.g. below 40 – 50 km for Guzewich & Smith, 2019). Their identification as water ice particles is robust, i.e., attempts to fit using dust properties are unable to reproduce the observed wavelength dependence of the derived  $k_{\text{ext}}$  (cf. figure 16). However, we have to keep in mind that our understanding of the spectral behaviour of the martian dust still needs to be improved, in particular about the hydration properties. Nevertheless, even updated dust optical properties are not expected to be able to reproduce the spectral bump observed in figure 16, as large water ice particles can do (cf. figure 6). These detections are found below smaller water ice particles (cf. figure 16, 3rd column). Although turbulence during dust storms is expected to enable the lifting of larger particles, the exact mechanism by which these large-grained water ice clouds form or are brought at high altitude remains to be investigated. In addition to turbulence, condensation nuclei properties could also play a role (Gooding, 1986; Michelangeli et al., 1993; Montmessin et al., 2004; Hartwick et al., 2019). One possibility is that these particles are not primarily composed of water ice but could host a relatively large dusty core. Incidentally, large dust particles have been reported from the surface during this GDS, (Lemmon et al., 2019), which could play a role as condensation nuclei for the water ice. Clancy et al. (2010) indeed observed during a previous GDS (2001) that large dust particles can propagate to high altitude (sizes between  $1 \mu\text{m}$  and  $2 \mu\text{m}$  above 70 km).

## 5 Conclusion

In this paper, we present our analyses of the Martian water ice clouds in the period before and during the MY 34 GDS using ACS infrared SO observations. This novel observational geometry in the mid-infrared allows us to monitor the  $3 \mu\text{m}$  water ice absorption band, and subsequently constrain the sizes of the detected water ice particles. Indeed, the shape of the wavelength profile of the  $3 \mu\text{m}$  absorption band is a sensitive function of the particle size. The sensitivity of this feature combined with the high resolution of ACS-MIR allows us to derive useful constraints on the particle size distribution of the clouds between  $r_{\text{eff}} \leq 0.1 \mu\text{m}$  and  $2 \mu\text{m}$ . Moreover, the temporal range of this dataset, from  $L_s = 165^\circ$  to  $L_s = 243^\circ$ , offers an unique opportunity to observe the impact of such a dust storm on the distribution and composition of the water ice clouds in the Martian atmosphere.

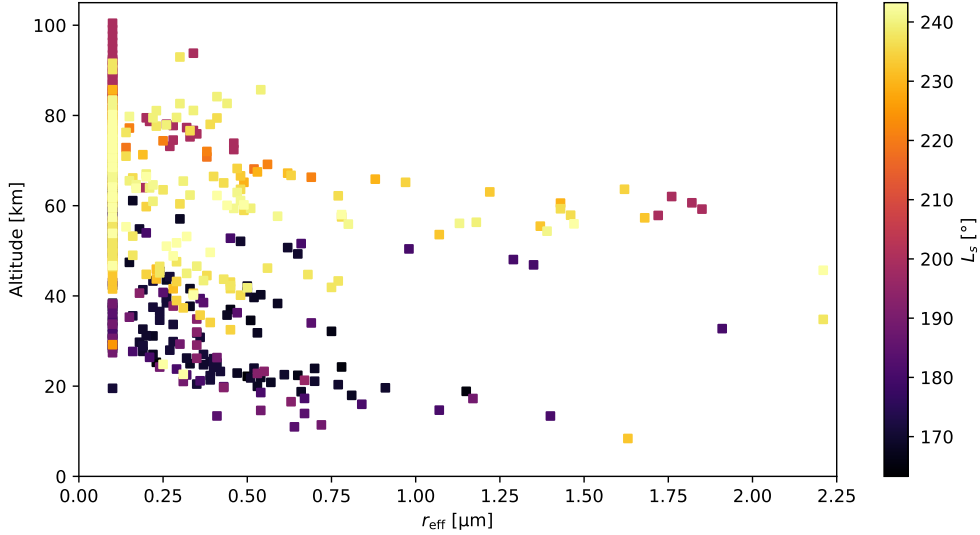


**Figure 13.** Distribution of the water ice particles size, as a function of the observed altitude and the Solar longitude. During the dust storm ( $L_s \geq 200^\circ$ ) the altitude of the water ice clouds increase, and they are mostly composed by smaller particles than before the dust storm (see also figure 15).

The main results are summarized below:

1. Using the ACS MIR dataset, we have developed of a method to identify water ice clouds, measure their opacity, and estimate their particle size. The method makes it possible to identify cloud for particle size smaller than  $2 \mu\text{m}$ .
2. We have derived vertical profiles of water ice clouds opacity and average particle size before and during the MY 34 GDS (from  $L_s = 165^\circ$  to  $L_s = 243^\circ$ ).
3. We detect water ice clouds in most of the observations across the planet except during the onset of the GDS (4/5 of our profiles show at least one detection of water ice, and half of the non-detections are located within the onset of the GDS).
4. We retrieve very high haze top altitudes during the GDS, notably at solar longitudes close to the onset with evidence for mesospheric clouds at altitudes  $\geq 90 \text{ km}$ , and even up to  $100 \text{ km}$  for the maximum haze top altitude. This suggests that GDS may elevates peak haze altitudes by 10 to 20 km compared to the typical perihelion storm season values.
5. We observe that there is a general trend of decreasing particle size with altitude for the whole dataset, and more specifically that the particle size within a given cloud/profile also decreases with altitude, typically from 1 to  $2 \mu\text{m}$  at the bottom of the cloud down to less than  $0.2 \mu\text{m}$  at the top.
6. We note a decrease in the mean water ice particle size during the GDS, with a median  $r_{\text{eff}}$  of  $0.3 \mu\text{m}$  for water ice particles before the storm that become  $\leq 0.1 \mu\text{m}$  during the dust storm. This is related to an increase of the average altitude of clouds during the GDS, with a higher proportion of mesospheric, small-grained water ice clouds.
7. Finally, we observe evidence for large water ice particles ( $r_{\text{eff}} \sim 1.5 - 2 \mu\text{m}$ ) at unexpectedly high altitudes during the GDS (between 50 km and 70 km).

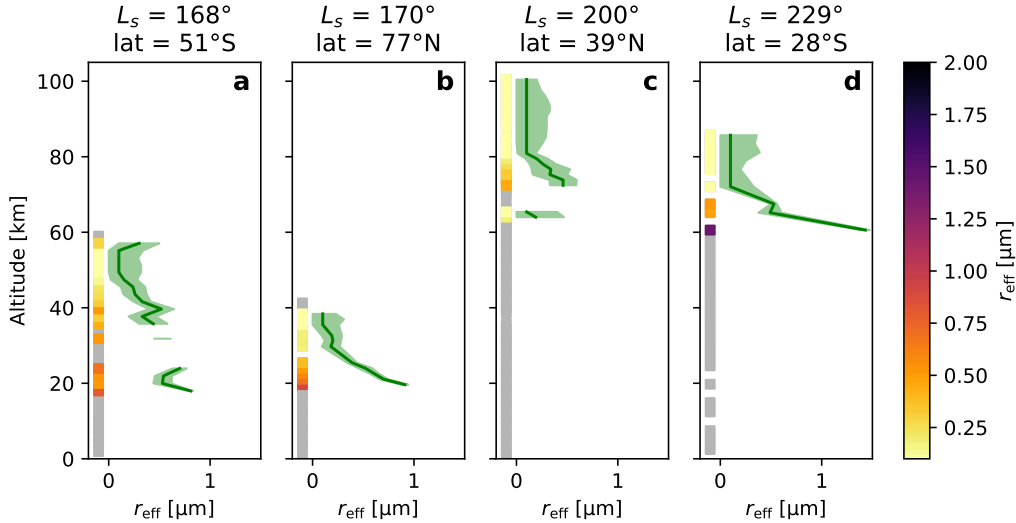


**Figure 14.** Typical vertical profiles of water ice clouds particle size before (a & b) and during (c & d) the GDS. Each panel represents the same profile in two manners: first the vertical line on the left where  $r_{\text{eff}}$  is represented using a color scale (same as figure 10); and second the green lines with  $r_{\text{eff}}$  on the x-axis and the uncertainties shown by the shadowed regions. We observe that the size of the water ice particles of the cloud decreases as the altitude increases, regardless of the mean altitude of the cloud. The GDS is characterized by a shift in altitude of the particle size distribution ( $\sim 30$  km higher, see profile c compared to a and b), along with a decrease of particles with size between  $0.5 \mu\text{m}$  and  $1 \mu\text{m}$  (cf. figure 15). But some GDS profiles show evidence of larger-grained layers ( $> 1 \mu\text{m}$ ) as we can see at 60 km in the profile d.

To conclude, this study shows that the MY 34 GDS has impacted the water ice clouds distribution, with more frequent clouds detections at very high altitudes up to above 90 km, along with evidence of unexpected particles with radii  $\geq 1.5 \mu\text{m}$  up to 70 km.

### Acknowledgments

ExoMars is a space mission of ESA and Roscosmos. The ACS experiment is led by IKI Space Research Institute in Moscow. The project acknowledges funding by Roscosmos and CNES. Science operations of ACS are funded by Roscosmos and ESA. Science support in IKI is funded by Federal agency of science organization (FANO). MJW acknowledge the support of the D’Alembert Fellowship program. Raw ACS data are available on the ESA PSA at <https://archives.esac.esa.int/psa/#!Table%20View/ACS=instrument>. Derived opacity and particles sizes can be found at <http://dx.doi.org/10.17632/w7yff8r97s.1>.

### References

- Audouard, J., Poulet, F., Vincendon, M., Milliken, R. E., Jouglet, D., Bibring, J.-P., ... Langevin, Y. (2014). Water in the Martian regolith from OMEGA/Mars Express. *Journal of Geophysical Research: Planets*, 119(8), 1969–1989. doi: 10.1002/2014JE004649
- Bevington, P. R., & Robinson, D. K. (1992). *Data reduction and error analysis for*

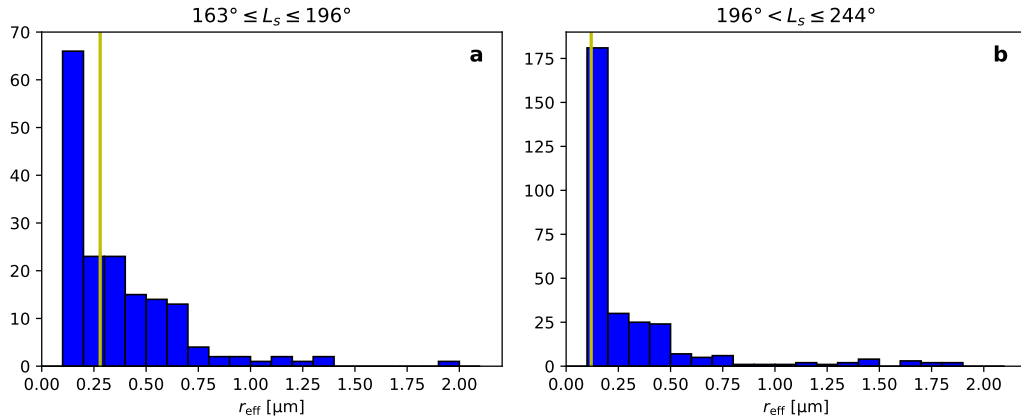


**Figure 15.** Distribution of the retrieved water ice particles sizes, before (a) and during (b) the MY 34 GDS. The yellow lines represent the median size for each distribution, respectively 0.28  $\mu\text{m}$  (a) and 0.1  $\mu\text{m}$  (b). We observe that during the dust storm we detect a fewer proportion of particle with a size between 0.5  $\mu\text{m}$  and 1  $\mu\text{m}$ , as most of our detection suggest sizes lower than 0.5  $\mu\text{m}$ , with a strong peak at 0.1  $\mu\text{m}$ . However, because we do not derive particles sizes lower than 0.1  $\mu\text{m}$ , the median  $r_{\text{eff}}$  value during the GDS must be consider as  $\leq 0.1 \mu\text{m}$  as more than half of our retrievals indicates sizes on the lower bounds of the models.

*the physical sciences - Second edition.* McGraw-Hill Inc.

Bibring, J.-P., Soufflot, A., Berth, M., Langevin, Y., Gondet, B., Drossart, P., ...

Forget, F. (2004, August). OMEGA: Observatoire pour la Minéralogie, l'Eau, les Glaces et l'Activité. *ESA Publication Division, 1240*, 37–49.

BIMP, IEC, IFCC, ILAC, ISO, IUPAC, ... OIML (2008). *JCGM 100: Evaluation of Measurement Data - Guide to the Expression of Uncertainty in Measurement* (Tech. Rep.). JCGM.

Calvin, W. M. (1997). Variation of the 3- $\mu\text{m}$  absorption feature on Mars: Observations over eastern Valles Marineris by the Mariner 6 infrared spectrometer. *Journal of Geophysical Research: Planets, 102*(E4), 9097–9107. doi: 10.1029/96JE03767

Chaffin, M. S., Deighan, J., Schneider, N. M., & Stewart, A. I. F. (2017, January). Elevated atmospheric escape of atomic hydrogen from Mars induced by high-altitude water. *Nature Geoscience, 10*, 174–178. doi: 10.1038/ngeo2887

Clancy, R. T., Grossman, A. W., Wolff, M. J., James, P. B., Rudy, D. J., Billawala, Y. N., ... Muhleman, D. O. (1996, July). Water Vapor Saturation at Low Altitudes around Mars Aphelion: A Key to Mars Climate? *Icarus, 122*(1), 36–62. doi: 10.1006/icar.1996.0108

Clancy, R. T., Sandor, B., Wolff, M., Lefvre, F., Navarro, T., Smith, M., ... Toigo, A. (2017, January). The Distribution of Mars Water Vapor Versus Altitude, Season, and Latitude as Derived from Global Comparisons of CRISM Retrieved and LMD GCM Simulated  $\text{O}_2(^1\text{g})$  Dayglow Profiles. In *The mars atmosphere: Modelling and observation* (p. 3203).

Clancy, R. T., Sandor, B. J., Wolff, M. J., Christensen, P. R., Smith, M. D., Pearl, J. C., ... Wilson, R. J. (2000). An intercomparison of ground-based millimeter, MGS TES, and Viking atmospheric temperature measurements: Seasonal and interannual variability of temperatures and dust loading in the global Mars atmosphere. *Journal of Geophysical Research: Planets, 105*(E4), 9553–9571. doi: 10.1029/1999JE001089

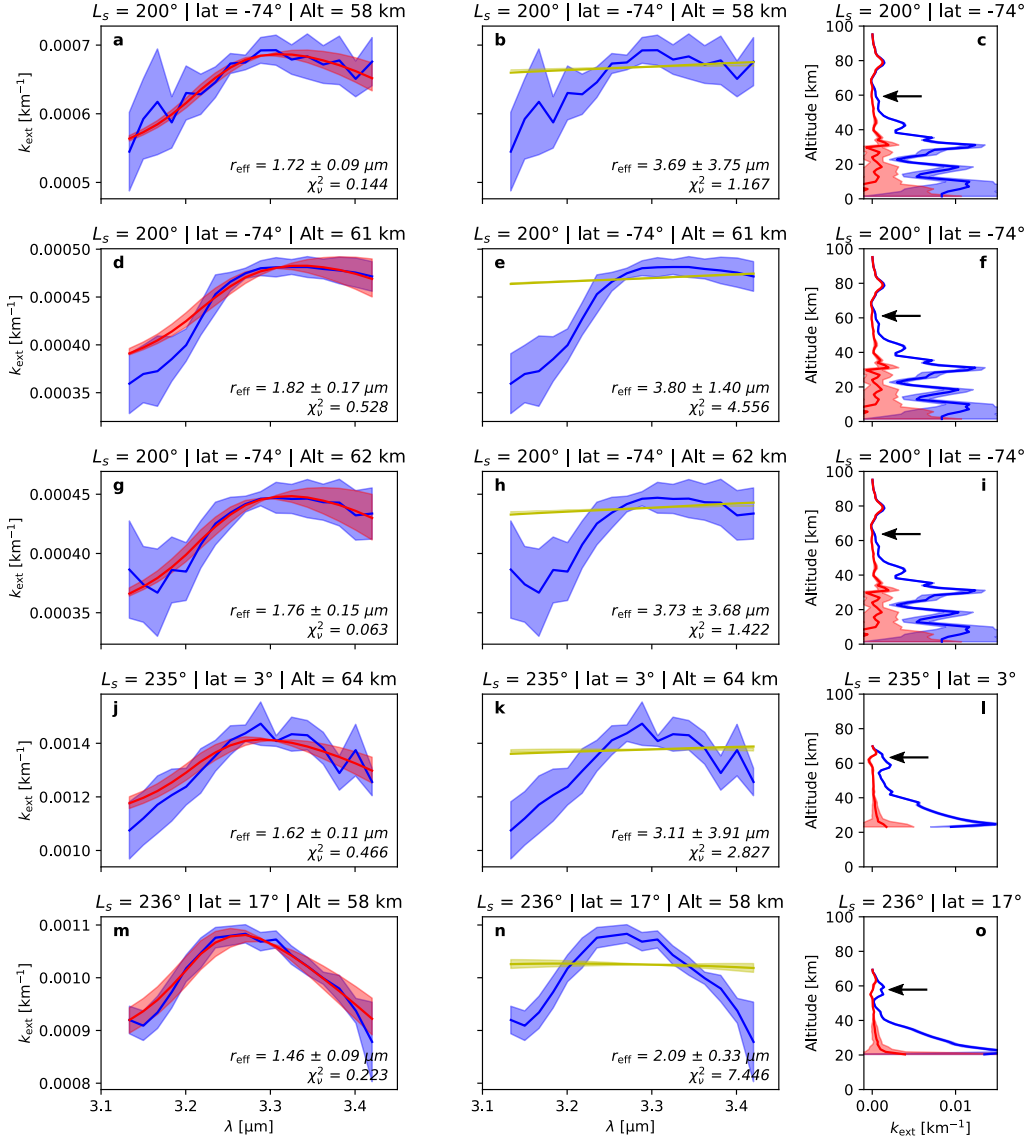


**Figure 16.** Big water ice particles ( $r_{\text{eff}} \geq 1.5 \mu\text{m}$ ) during the GDS. The two first columns shows the results of the fitting algorithm using the water ice model (left column) or the dust model (center column). The blue area represents the ACS-MIR spectra, while the red and yellow lines represent respectively the best fit using the water ice and dust models. The right column shows for each observation (line) the associated  $k_{\text{ext}}$  vertical profile (in blue the extinction coefficient at  $3.2 \mu\text{m}$ , and in red the difference between the extinction coefficient at  $3.2 \mu\text{m}$  and  $3.4 \mu\text{m}$ ). The black arrows indicate the altitude of the big particle observation. We can see in this figure that the detection of these large water ice particles is robust, as the full-dust model is not able to reproduce the observed spectra, especially the bump of extinction coefficient with the wavelength.

Clancy, R. T., Wolff, M. J., Smith, M. D., Kleinböhl, A., Cantor, B. A., Murchie, S. L., ... Sandor, B. J. (2019, August). The distribution, composition, and particle properties of Mars mesospheric aerosols: An analysis of CRISM



- visible/near-IR limb spectra with context from near-coincident MCS and MARCI observations. *Icarus*, *328*, 246–273. doi: 10.1016/j.icarus.2019.03.025
- Clancy, R. T., Wolff, M. J., Whitney, B. A., Cantor, B. A., Smith, M. D., & McConnochie, T. H. (2010, May). Extension of atmospheric dust loading to high altitudes during the 2001 Mars dust storm: MGS TES limb observations. *Icarus*, *207*(1), 98–109. doi: 10.1016/j.icarus.2009.10.011
- Crismani, M. M. J., Schneider, N. M., Plane, J. M. C., Evans, J. S., Jain, S. K., Chaffin, M. S., . . . Jakosky, B. M. (2017, June). Detection of a persistent meteoric metal layer in the Martian atmosphere. *Nature Geoscience*, *10*, 401–404. doi: 10.1038/ngeo2958
- Fedorova, A., Bertaux, J.-L., Betsis, D., Montmessin, F., Korablev, O., Maltagliati, L., & Clarke, J. (2018, January). Water vapor in the middle atmosphere of Mars during the 2007 global dust storm. *Icarus*, *300*, 440–457. doi: 10.1016/j.icarus.2017.09.025
- Fedorova, A., Montmessin, F., Korablev, O., Luginin, M., Trokhimovskiy, A., Belyaev, D. A., . . . Wilson, C. F. (2020, January). Stormy water on Mars: The distribution and saturation of atmospheric water during the dusty season. *Science*, eaay9522. doi: 10.1126/science.aay9522
- Forget, F., Hourdin, F., Fournier, R., Hourdin, C., Talagrand, O., Collins, M., . . . Huot, J.-P. (1999). Improved general circulation models of the Martian atmosphere from the surface to above 80 km. *Journal of Geophysical Research: Planets*, *104*(E10), 24155–24175. doi: 10.1029/1999JE001025
- Goldman, A., & Saunders, R. (1979, February). Analysis of atmospheric infrared spectra for altitude distribution of atmospheric trace constituents I. Method of analysis. *Journal of Quantitative Spectroscopy and Radiative Transfer*, *21*(2), 155–161. doi: 10.1016/0022-4073(79)90027-X
- Gooding, J. L. (1986, April). Martian dust particles as condensation nuclei: A preliminary assessment of mineralogical factors. *Icarus*, *66*(1), 56–74. doi: 10.1016/0019-1035(86)90006-0
- Guzewich, S. D., Lemmon, M., Smith, C. L., Martínez, G., VicenteRetortillo, . d., Newman, C. E., . . . Mier, M.-P. Z. (2019, January). Mars Science Laboratory Observations of the 2018/Mars Year 34 Global Dust Storm. *Geophysical Research Letters*, *46*, 71–79. doi: 10.1029/2018GL080839
- Guzewich, S. D., & Smith, M. D. (2019, February). Seasonal Variation in Martian Water Ice Cloud Particle Size. *Journal of Geophysical Research: Planets*, *124*(2), 636–643. doi: 10.1029/2018JE005843
- Guzewich, S. D., Smith, M. D., & Wolff, M. J. (2014, December). The vertical distribution of Martian aerosol particle size: Vertical Profile of Mars Aerosol Size. *Journal of Geophysical Research: Planets*, *119*(12), 2694–2708. doi: 10.1002/2014JE004704
- Hanel, R., Conrath, B., Hovis, W., Kunde, V., Lowman, P., Maguire, W., . . . Burke, T. (1972, October). Investigation of the Martian environment by infrared spectroscopy on Mariner 9. *Icarus*, *17*(2), 423–442. doi: 10.1016/0019-1035(72)90009-7
- Hansen, J. E., & Travis, L. D. (1974, October). Light scattering in planetary atmospheres. *Space Science Reviews*, *16*(4), 527–610. doi: 10.1007/BF00168069
- Hartwick, V. L., Toon, O. B., & Heavens, N. G. (2019, July). High-altitude water ice cloud formation on Mars controlled by interplanetary dust particles. *Nature Geoscience*, *12*(7), 516–521. doi: 10.1038/s41561-019-0379-6
- Heavens, N. G., Kleinbhl, A., Chaffin, M. S., Halekas, J. S., Kass, D. M., Hayne, P. O., . . . Schofield, J. T. (2018, February). Hydrogen escape from Mars enhanced by deep convection in dust storms. *Nature Astronomy*, *2*(2), 126–132. doi: 10.1038/s41550-017-0353-4
- Heavens, N. G., Richardson, M. I., Kleinböhl, A., Kass, D. M., McCleese, D. J., Abdou, W., . . . Wolkenberg, P. M. (2011). The vertical distribution of

- dust in the Martian atmosphere during northern spring and summer: Observations by the Mars Climate Sounder and analysis of zonal average vertical dust profiles. *Journal of Geophysical Research: Planets*, 116(E4). doi: 10.1029/2010JE003691
- Jaquin, F., Gierasch, P., & Kahn, R. (1986, December). The vertical structure of limb hazes in the Martian atmosphere. *Icarus*, 68(3), 442-461. doi: 10.1016/0019-1035(86)90050-3
- Jouglet, D., Poulet, F., Milliken, R. E., Mustard, J. F., Bibring, J.-P., Langevin, Y., ... Gomez, C. (2007). Hydration state of the Martian surface as seen by Mars Express OMEGA: 1. Analysis of the 3 m hydration feature. *Journal of Geophysical Research: Planets*, 112(E8). doi: 10.1029/2006JE002846
- Kass, D., Schofield, J., Kleinböhl, A., McCleese, D., Heavens, N., Shirley, J., & Steele, L. (2019, September). Mars Climate Sounder observation of Mars' 2018 global dust storm. *Geophysical Research Letters*. doi: 10.1029/2019GL083931
- Kass, D. M., Kleinböhl, A., McCleese, D. J., Schofield, J. T., & Smith, M. D. (2016, June). Interannual similarity in the Martian atmosphere during the dust storm season. *Geophysical Research Letters*, 43(12), 6111-6118. doi: 10.1002/2016GL068978
- Kleinböhl, A., Schofield, J. T., Kass, D. M., Abdou, W. A., Backus, C. R., Sen, B., ... McCleese, D. J. (2009, October). Mars Climate Sounder limb profile retrieval of atmospheric temperature, pressure, and dust and water ice opacity. *Journal of Geophysical Research: Planets*, 114(E10). doi: 10.1029/2009JE003358
- Korablev, O., Montmessin, F., Trokhimovskiy, A., Fedorova, A. A., Shakun, A. V., Grigoriev, A. V., ... Zorzano, M. P. (2018, February). The Atmospheric Chemistry Suite (ACS) of Three Spectrometers for the ExoMars 2016 Trace Gas Orbiter. *Space Science Reviews*, 214, 7. doi: 10.1007/s11214-017-0437-6
- Korablev, O., Vandaele, A. C., Montmessin, F., Fedorova, A. A., Trokhimovskiy, A., Forget, F. c., ... The ACS and NOMAD Science Teams (2019, April). No detection of methane on Mars from early ExoMars Trace Gas Orbiter observations. *Nature*, 568, 517-520. doi: 10.1038/s41586-019-1096-4
- Lemmon, M. T., Guzewich, S. D., McConnochie, T., Vicente-Retortillo, A., Martínez, G., Smith, M. D., ... Jacob, S. (2019, August). Large Dust Aerosol Sizes Seen During the 2018 Martian Global Dust Event by the Curiosity Rover. *Geophysical Research Letters*. doi: 10.1029/2019GL084407
- Madeleine, J.-B., Forget, F., Spiga, A., Wolff, M. J., Montmessin, F., Vincendon, M., ... Schmitt, B. (2012, November). Aphelion water-ice cloud mapping and property retrieval using the OMEGA imaging spectrometer onboard Mars Express: OMEGA ANALYSIS OF MARS WATER ICE CLOUDS. *Journal of Geophysical Research: Planets*, 117(E11). doi: 10.1029/2011JE003940
- Maltagliati, L., Montmessin, F., Fedorova, A., Korablev, O., Forget, F., & Bertaux, J.-L. (2011, September). Evidence of Water Vapor in Excess of Saturation in the Atmosphere of Mars. *Science*, 333(6051), 1868-1871. doi: 10.1126/science.1207957
- Michelangelo, D. V., Toon, O. B., Haberle, R. M., & Pollack, J. B. (1993, April). Numerical Simulations of the Formation and Evolution of Water Ice Clouds in the Martian Atmosphere. *Icarus*, 102(2), 261-285. doi: 10.1006/icar.1993.1048
- Montmessin, F., Forget, F., Rannou, P., Cabane, M., & Haberle, R. M. (2004). Origin and role of water ice clouds in the Martian water cycle as inferred from a general circulation model. *Journal of Geophysical Research: Planets*, 109(E10). doi: 10.1029/2004JE002284
- Montmessin, F., Quémerais, E., Bertaux, J. L., Korablev, O., Rannou, P., & Lebonnois, S. (2006). Stellar occultations at UV wavelengths by the SPICAM instrument: Retrieval and analysis of Martian haze profiles. *Journal of Geophysical Research*, 111(E9). doi: 10.1029/2005JE002662

- Murchie, S., Arvidson, R., Bedini, P., Beisser, K., Bibring, J.-P., Bishop, J., ... Wolff, M. (2007). Compact Reconnaissance Imaging Spectrometer for Mars (CRISM) on Mars Reconnaissance Orbiter (MRO). *Journal of Geophysical Research: Planets*, 112(E5). doi: 10.1029/2006JE002682
- Navarro, T., Forget, F., Millour, E., & Greybush, S. J. (2014). Detection of detached dust layers in the Martian atmosphere from their thermal signature using assimilation. *Geophysical Research Letters*, 41(19), 6620-6626. doi: 10.1002/2014GL061377
- Neary, L., Daerden, F., Aoki, S., Whiteway, J., Clancy, R., Smith, M., ... Vandaele, A. (2019, September). Explanation for the increase in high altitude water on Mars observed by NOMAD during the 2018 global dust storm. *Geophysical Research Letters*. doi: 10.1029/2019GL084354
- Plane, J. M. C., Carrillo-Sanchez, J. D., Mangan, T. P., Crismani, M. M. J., Schneider, N. M., & Määttänen, A. (2018). Meteoric Metal Chemistry in the Martian Atmosphere. *Journal of Geophysical Research: Planets*, 123(3), 695-707. doi: 10.1002/2017JE005510
- Richardson, M. I. (2002). Water ice clouds in the Martian atmosphere: General circulation model experiments with a simple cloud scheme. *Journal of Geophysical Research*, 107(E9). doi: 10.1029/2001JE001804
- Sánchez-Lavega, A., del Río-Gaztelurrutia, T., Hernández-Bernal, J., & Delcroix, M. (2019). The Onset and Growth of the 2018 Martian Global Dust Storm. *Geophysical Research Letters*, 46(11), 6101-6108. doi: 10.1029/2019GL083207
- Smith, M. D. (2004, January). Interannual variability in TES atmospheric observations of Mars during 1999–2003. *Icarus*, 167(1), 148–165. doi: 10.1016/j.icarus.2003.09.010
- Smith, M. D. (2019, November). THEMIS observations of the 2018 Mars global dust storm. *Journal of Geophysical Research: Planets*. doi: 10.1029/2019JE006107
- Smith, M. D., Wolff, M. J., Clancy, R. T., Kleinböhl, A., & Murchie, S. L. (2013, February). Vertical distribution of dust and water ice aerosols from CRISM limb-geometry observations. *Journal of Geophysical Research: Planets*, 118(2), 321–334. doi: 10.1002/jgre.20047
- Szantai, A., Audouard, J., Forget, F., Olsen, K. S., Gondet, B., Millour, E., ... Bibring, J.-P. (2019, April). Martian cloud climatology and life cycle extracted from Mars Express OMEGA spectral images. *arXiv e-prints*, arXiv:1904.06422.
- Toon, O. B., & Ackerman, T. P. (1981, October). Algorithms for the calculation of scattering by stratified spheres. *Applied Optics*, 20(20), 3657. doi: 10.1364/AO.20.003657
- Trokhimovskiy, A., Korablev, O., Ivanov, Y. S., Siniyavsky, I. I., Fedorova, A., Stepanov, A. V., ... Montmessin, F. (2015, September). Middle-infrared echelle cross-dispersion spectrometer ACS-MIR for the ExoMars Trace Gas Orbiter. In *Infrared remote sensing and instrumentation XXIII* (Vol. 9608, p. 960808). doi: 10.1117/12.2190359
- Vals, M., Forget, F., Spiga, A., & Millour, E. (2018, September). Impact of the refinement of the vertical resolution on the simulation of the water cycle by the martian LMD Global Climate Model. In (Vol. 12, p. EPSC2018-847).
- Vandaele, A. C., Korablev, O., Daerden, F., Aoki, S., Thomas, I. R., Altieri, F., ... ACS Science Team (2019, April). Martian dust storm impact on atmospheric H<sub>2</sub>O and D/H observed by ExoMars Trace Gas Orbiter. *Nature*, 568, 521–525. doi: 10.1038/s41586-019-1097-3
- Vandaele, A. C., Lopez-Moreno, J.-J., Patel, M. R., Bellucci, G., Daerden, F., Ristic, B., ... the NOMAD Team (2018, August). NOMAD, an Integrated Suite of Three Spectrometers for the ExoMars Trace Gas Mission: Technical Description, Science Objectives and Expected Performance. *Space Science Reviews*, 214(5). doi: 10.1007/s11214-018-0517-2

- Vincendon, M., Pilorget, C., Gondet, B., Murchie, S., & Bibring, J.-P. (2011, November). New near-IR observations of mesospheric CO<sub>2</sub> and H<sub>2</sub>O clouds on Mars. *Journal of Geophysical Research*, *116*, E00J02. doi: 10.1029/2011JE003827
- Virtanen, P., Gommers, R., Oliphant, T. E., Haberland, M., Reddy, T., Cournapeau, D., . . . Contributors, S. . . (2019, July). SciPy 1.0—Fundamental Algorithms for Scientific Computing in Python. *arXiv:1907.10121 [physics]*.
- Wang, H., & Richardson, M. I. (2015, May). The origin, evolution, and trajectory of large dust storms on Mars during Mars years 2430 (19992011). *Icarus*, *251*, 112–127. doi: 10.1016/j.icarus.2013.10.033
- Wilson, R. J., Lewis, S. R., Montabone, L., & Smith, M. D. (2008). Influence of water ice clouds on Martian tropical atmospheric temperatures. *Geophysical Research Letters*, *35*(7). doi: 10.1029/2007GL032405
- Wolff, M. J., & Clancy, R. T. (2003). Constraints on the size of Martian aerosols from Thermal Emission Spectrometer observations. *Journal of Geophysical Research: Planets*, *108*(E9). doi: 10.1029/2003JE002057
- Wolff, M. J., Clancy, R. T., Kahre, M. A., Haberle, R. M., Forget, F., Cantor, B. A., & Malin, M. C. (2019, November). Mapping water ice clouds on Mars with MRO/MARCI. *Icarus*, *332*, 24–49. doi: 10.1016/j.icarus.2019.05.041
- Wolff, M. J., López-Valverde, M., Madeleine, J.-B., Wilson, R. J., Smith, M. D., Fouchet, T., & Delory, G. T. (2017). Radiative Process: Techniques and Applications. In R. M. Haberle et al. (Eds.), *The atmosphere and climate of Mars* (p. 76–105). Cambridge University Press. doi: 10.1017/9781139060172.006
- Zurek, R. W., & Martin, L. J. (1993, February). Interannual variability of planet-encircling dust storms on Mars. *Journal of Geophysical Research: Planets*, *98*(E2), 3247–3259. doi: 10.1029/92JE02936